Ultrafast Electron Tunneling Devices—From Electric-Field Driven to Optical-Field Driven

Shenghan Zhou, Ke Chen, Matthew Thomas Cole, Zhenjun Li, Mo Li, Jun Chen, Christoph Lienau, Chi Li,* and Qing Dai**

The search for ever higher frequency information processing has become an area of intense research activity within the micro, nano, and optoelectronics communities. Compared to conventional semiconductor-based diffusive transport electron devices, electron tunneling devices provide significantly faster response times due to near-instantaneous tunneling that occurs at sub-femtosecond timescales. As a result, the enhanced performance of electron tunneling devices is demonstrated, time and again, to reimagine a wide variety of traditional electronic devices with a variety of new "lightwave electronics" emerging, each capable of reducing the electron transport channel transit time down to attosecond timescales. In response to unprecedented rapid progress within this field, here the current state-of-the-art in electron tunneling devices is reviewed, current challenges and opportunities are highlighted, and possible future research directions are identified.

1. Introduction

Microelectronics remain the bedrock of our modern digital age. However, due to continued device miniaturization, modern electronics experience two technologically challenging and functionally significant bottlenecks: speed limitation and high power consumption.[1] Both challenges are principally linked to electron–phonon interactions during transport in conventional semiconductor channels. New approaches to device fabrication, capable of supporting alternative modes of electron transport, are urgently required to allow for continued speed improvements whilst concurrently reducing power consumption. Electron tunneling devices represent one class of solution. They can simultaneously realize ultrafast response at attosecond (10^{-18} s) timescale, low power consumption, and miniaturization, which are likely to manifest through the fusion of conventional solid-state electronics and vacuum electronic devices.[2]

Due to the inherently limited switching speed of electronics driving systems, it remains challenging to achieve sub-picosecond (10^{-12} s) response times with conventional electrically driven electron tunneling devices. The use of ultrafast lasers for optical-field-driven tunneling devices has established one important way to breakthrough this technologically time limit.[3–5] The quantum mechanical tunneling of electrons through a potential barrier involves almost no scattering and negligible energy loss and occurs over sub-optical-cycle frame—attosecond time (10^{-18}) timescale.[3,4,6,7] Nonlinearity in the ultrafast tunneling process can convert the sub-optical-cycle response into a technologically useful direct current. These optical-field-driven electron tunneling devices have the potential for much wider use in on-chip "lightwave electronics."[8–16]

Recently, a variety of novel low-dimensional, commonly carbon-based, nanomaterials, have been used in electron tunneling devices and have been seen to provide a platform with

---

S. H. Zhou, K. Chen, Dr. Z. J. Li, Prof. C. Li, Prof. Q. Dai
CAS Key Laboratory of Nanophotonic Materials and Devices
CAS Key Laboratory of Standardization and Measurement
for Nanotechnology
CAS Center for Excellence in Nanoscience
National Center for Nanoscience and Technology
Beijing 100190, P. R. China
E-mail: lichi@nanoctr.cn; daiq@nanoctr.cn

S. H. Zhou, K. Chen, Dr. Z. J. Li, Prof. C. Li, Prof. Q. Dai
Center of Materials Science and Optoelectronics Engineering
University of Chinese Academy of Sciences
Beijing 100049, P. R. China

Dr. M. T. Cole
Department of Electronic and Electrical Engineering
University of Bath
Bath BA2 7AY, UK

Prof. M. Li
School of Electronic Science and Engineering
University of Electronic Science and Technology of China
Chengdu 611731, P. R. China

Prof. J. Chen
State Key Laboratory of Optoelectronic Materials and Technologies
Guangdong Province Key Laboratory of Display Material and Technology
School of Electronics and Information Technology
Sun Yat-sen University
Guangzhou 510275, P. R. China

Prof. C. Lienau
Institut für Physik
Center of Interface Science
Carl von Ossietzky Universität
26129 Oldenburg, Germany
E-mail: christoph.lienau@uni-oldenburg.de

significant potential for high-speed devices. With rapid advancements in the growth and integration of low-dimensional nanomaterials, many of which having tailor-designed band-structures,[17,18] a wide variety of emerging tunneling devices have come to the fore, each exhibiting superior performance in contrast to continuous band-structured traditional materials. It is widely believed that electron tunneling devices, when aligned with the provision of engineered low-dimensional nanomaterial systems, will drive a more-than-Moore future, allowing for the development of new and functionally novel nanoelectronic architectures capable of concurrent high-speed and low-power consumption.

Here, we summarize the present state-of-the-art in this emerging and rapidly evolving field. We first review the operation principles of electric-field-driven tunneling and optical-field-driven tunneling based on different tunneling mechanisms, including direct tunneling, resonant tunneling, and inelastic tunneling. Then, we discuss current developments of electric-field-driven electron tunneling devices, focusing on the materials and device architectures. Finally, we provide an outline of some of the most recent demonstrations of optical-field-driven tunneling devices and some brief outlooks into the future directions of this field.

2. Principles of Electron Tunneling

In this section, the operation principles of electric-field-driven tunneling and optical-field-driven tunneling are summarized, including direct tunneling, resonant tunneling, and inelastic tunneling.

2.1. Electric-Field-Driven Tunneling

2.1.1. Direct Tunneling

Metal–insulator–metal (MIM) multilayer structures are one of the most structurally simple, and hence most widely investigated, types of tunneling devices. The band diagram of a typical direct tunneling MIM structure is shown in **Figure 1**a. Here, the electrons from the surface of the left metal can tunnel directly through the energy barrier formed by the dielectric layer. For thick dielectrics, direct tunneling is little noticed in the transport profile, direct tunneling dominates electron transport as the dielectric layer gets increasingly thin, especially for sub-10 nm dielectrics. With research spanning more than four decades, MIM devices are comparatively mature technology. MIMs find use mainly in electronic components such as double-gate tunneling field-effect transistors (FETs) and high-*k* gate dielectric tunneling FETs.[19,20] Though capable of being modeled by a wide range of transport models, that depend critically on a variety of material and device structural properties, the Fowler-Nordheim (F-N) tunneling model is perhaps the most commonly used, though not strictly correct or most appropriate model for direct tunneling. As depicted in Figure 1b, in the F-N model the electrons do not tunnel directly to the other side of the barrier. Rather, they tunnel from the surface of the left metal to the conduction band (CB) of the insulator. The F-N tunneling regime is significant for thicker dielectrics and sufficiently high electric fields. In the case when the dielectric is a vacuum, a metal–vacuum–metal (MVM) structure is formed. The exploration of these nanoscale vacuum-channel diodes (NVDs) is another recently hot research

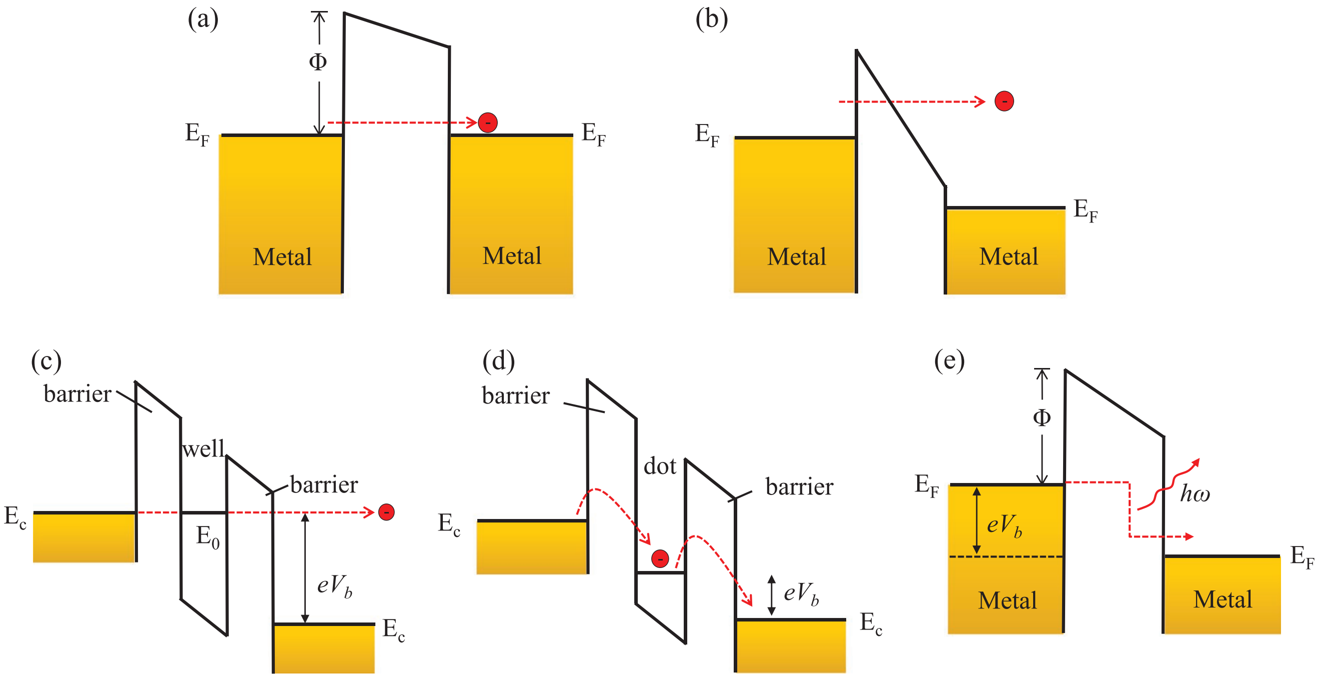

Figure 1. The principles of electric-field-driven tunneling. a) Energy band diagram for direct tunneling. E_F, Fermi level; Φ, barrier height; V_G, gate voltage. b) Energy band diagram for F-N tunneling. c) Energy band diagram for resonant tunneling. E_c, Fermi level of the electrode; E_0, Fermi level of the potential well; V_b, applied bias. d) Energy band diagram of single-electron tunneling devices. The electron can only tunnel through the barrier one by one due to Coulomb blockade effects. e) Energy band diagram for inelastic tunneling during photon emission. $\hbar\omega$, photon energy.

topic.[21–26] NVDs inherit many of the functional advantages of traditional, often bulky vacuum electronic devices, such as high operation frequency and high output power, as well as many of the production benefits associated with conventional silicon integrated circuitry. NVDs are well positioned to capitalize on the merits of both established communities, particularly as the channel length becomes less than the electrons mean free path in air, the technologically demanding and bulky vacuum environments in traditional device becomes unnecessary supporting the realization of air-operation devices.

2.1.2. Resonant Tunneling

Since the 1970s, resonant tunneling devices have attracted significant attention for their use in radio frequency oscillators, multivalued logic, high-frequency radar, communication systems, and signal processing.[27–32] Figure 1c shows an energy band diagram of a typical resonant tunneling device. When a bias voltage V_b is applied, for which the Fermi level E_c of the top electrode matches the quantum well energy level E_0, resonant tunneling can be established and a local maximum in the conductance occurs, evidenced as a peak in the measured current–voltage (I–V) profiles. Resonant tunneling of charge carriers between two spatially separated quantum states can lead to negative differential resistance (NDR),[33,34] which is a key feature in novel nanoelectronics circuits. High currents can be achieved at low voltages through band engineering in resonant tunneling devices due to the ability to engineer the quantum wells within the material.

Single-electron tunneling is a special case of resonant tunneling where the electrons are transported one by one through a quantum dot (QD). Single-electron tunneling devices operate via a capacitive charging energy (i.e., classical Coulomb blockade effect), which makes it possible to inject controllably, at well-defined energies, single carriers into quantum dots. Single-electron tunneling devices have garnered great attention because of their concurrent high-speed and low-power operation, and specifically for their potential deployment in emerging qubit applications.[35–38] Figure 1d shows a typical energy band diagram of a single-electron tunneling device. When the Fermi level of the top electrode matches the QD energy level, only one electron can tunnel into the unoccupied levels of the QD from the top electrode through the barrier. This electron then tunnels into the bottom electrode when the Fermi level of the bottom electrode is equal to the QD energy level. This electrical characteristic of the single-electron tunneling phenomenon has been extensively characterized and is well described based on double-barrier tunneling junction.[39,40]

2.1.3. Inelastic Tunneling

Electrons commonly interact with various quasi-particles, such as phonons, plasmons, and magnons, particularly in solid-channel devices, such as MIMs. In these processes, inelastic tunneling channels may open, usually accompanied by energy loss, and photons may be generated. Inelastic tunneling has been used widely in materials characterization as well as, more recently, in signal generation, transmission, modulation, and detection in photonic integrated devices.[41–50] Figure 1e shows an energy band diagram of an electric-field-driven inelastic tunneling device during photon emission. When biased, the electrons tunnel through the barrier layer to another metal electrode. This process results in stimulated photon emission. The tunneling current includes contributions from both elastic and inelastic electrons. The majority of the electrons tunnel elastically without energy loss. Of the remaining electrons, a significantly smaller proportion inelastically tunnel through the barrier and lose energy such that $\hbar\omega \leq eV_b$, where $\hbar$ is the reduced Plank constant, ω is the angular frequency of the optical mode, and V_b is a bias voltage.[51] This energy loss excites localized plasmon modes, often termed "gap plasmons."[52,53] These plasmons decay through various relaxation pathways, including radiative or nonradiative mechanisms which allow device engineers to create novel device architectures that draw function from these nonideal transport modes.

2.2. Optical-Field-Driven Tunneling

The underlying mechanism of optical-induced tunneling includes thermal-induced tunneling[54,55] and photoinduced tunneling.[56] Under these regimes, electrons are first excited from their original energy level to a higher energy-level state by absorbing thermal (thermally induced tunneling) or one photon energy (single-photon tunneling). They then face a much narrower tunneling barrier, which results in an enhanced emission current. However, all such excitation methodologies do not support femtosecond response times. Ultrafast femtosecond laser-assisted electron tunneling is considered the primary candidate for reaching femtosecond and even attosecond response times. As shown in **Figure 2**, upon illumination with an intense ultrafast laser pulse an electron may emit through the barrier in two ways. First, as shown in Figure 2a, electrons in the Fermi level may absorb more than one photon and gain sufficient energy to overcome the barrier height. This is commonly referred to as multiphoton tunneling.[57] Here, the electron yield follows an Nth power of the laser intensity, where N is the nonlinear order in the absorption processes. The timescale for the multiphoton photoemission follows the width of the laser pulse divided by $N^{1/2}$. Under the influence of a stronger laser field, moving beyond the multiphoton regime, the barrier allows penetration, and subsequent tunneling emission, only in a short period of each cycle of the laser pulse.[58] In this strong optical-field regime, the time duration of generated electron wavepackets consists of a series of bunches, separated by the cycle period and each shorter than half-cycle of the incident field, as shown in Figure 2b. In particular, the use of an ultrafast few-cycled laser can generate tunneling electron wavepackets of sub-femtosecond time duration,[3–5,7] which is the basis for achieving attosecond electron transport in nanoscale channels. Photoemission may transition into optical-field emission (OFE) from the multiphoton emission regime with increasing optical field strength. This transition can be described by the Keldysh framework.[59] The Keldysh framework introduces a characteristic parameter γ that separates the two photoemission regimes, a multiphoton emission regime[60] ($\gamma \geq 1$) and a strong optical-field

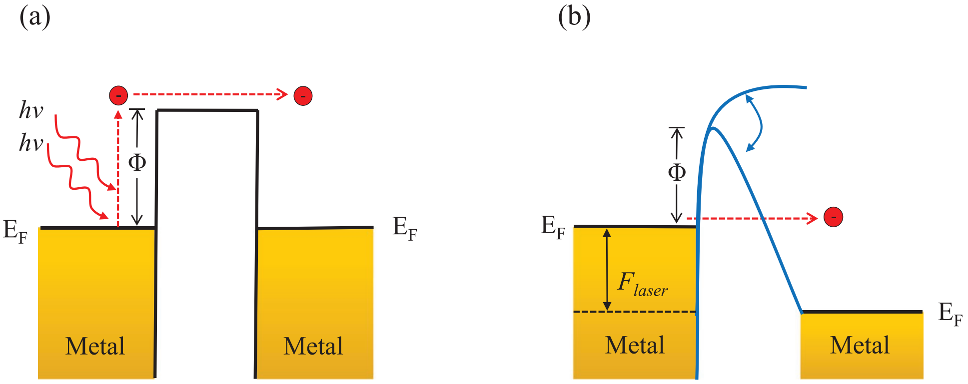

Figure 2. Mechanisms of optical-field-driven tunneling. a) Multiphoton emission. An electron absorbs the energy of a number of photons to overcome the barrier for photoemission. E_F, Fermi level; Φ, barrier height. b) Optical-field tunneling emission. A strong optical field induces a periodically oscillating barrier at an optical-frequency of ω. When the optical field is strong enough to create a penetrable tunneling barrier, electrons tunnel from the Fermi level in a fraction of a negative half optical-cycle.

tunneling emission regime[61] ($\gamma \leq 1$). The Keldysh parameter $\gamma = \omega\sqrt{2m\varphi}/e\beta F$, where ω is the optical-frequency; φ is the barrier height; m and e are the mass and charge of the electron, respectively; F is the incident light-field strength; β is the field-enhancement factor of the emitter.

According to established strong-field physics,[3,4] following the optical-field-driven tunneling process, the electrons are accelerated by the strong optical-field in the near-field of the emitting surface. Hommelhoff et al.[3] demonstrated carrier-envelope phase (CEP) sensitive high-order photoelectron emission from a W nanotip, with a current modulation of up to 100%. The highly nonlinear phenomenon is attributed to the interference of electron wavepackets that are coherently emitted during two adjacent optical-cycles. Ropers et al.[4] observed sub-optical-cycle acceleration in an Au nanotip; a novel form of quiver-quenched electron motion in the strong optical-field regime. Lienau et al.[5] clarified, for the first time, the effect of the optical-fields CEP on the generation and motion of strong-field-emitted electrons from sharp Au tips. Such field-driven control of electron motion in solid-state nanostructures will pave the way toward new approaches for the generation, measurement, and application of attosecond electron pulses. For a recent overview, we refer the reader to refs. [61, 62]. However, optical-field-driven electron dynamics in nanoscale transport volumes remain unclear with much research required, to lay much needed foundations for a new generation of lightwave electronic devices.

3. Recent Developments of Electric-Field-Driven Tunneling Devices

3.1. Direct Tunneling Devices

In this section, we summarize recent developments in MIM and MVM devices in the direct tunneling regime.

3.1.1. Direct Tunneling Devices Based on Traditional Materials

Direct tunneling devices can be divided into bipolar (diodes, formed from two sharp tips),[25] or tertiary (triodes) structures that include additional side[26] or bottom-gates.[24,63] The primary advantage of triodes is their ability to finely control the emission by adjustment of the gate voltage. When the gate voltage is less than the turn-on voltage, a small proportion of the electron population is emitted over the barrier due to thermal excitation linked to the energy spread of the electron populations; the emitted current, however, remains low. As the gate voltage increases beyond the turn-on voltage, the vacuum energy level bends downward, thus enabling an increasing number of electrons to tunnel through the narrowed potential barrier leading to a dramatic increase in current as soon as the device enters its high-current, low-resistance on-state. In 2012, Meyyappan et al.[24] demonstrated a planar back-gate FET whose cutoff frequency was 0.46 THz, ten times greater than comparable semiconductor devices. They predicted that this tunneling structure can potentially improve the cutoff frequency well into the THz regime by process and layout refinements, which, in part, continue to drive the rapid expansion of research on tunneling electronic devices. Nevertheless, non-negligible current leakage to triode gates has proven a long-standing issue.[24,26] Recently, to reduce gate leakage current and improve device performance, the same team demonstrated a tunneling transistor consisting of an atomically sharp source and drain electrode embedded in a nanoscale surrounding gate.[16,22,23] **Figure 3**a shows the structure of a typical surround-gate electron tunneling device. The gate leakage current was 10^6 times smaller than the drain current, confirming that the surround-gate dielectric effectively inhibits leakage.

Recently, Sriram et al.[21] demonstrated a new metal-based nanoscale air-channel tunneling device. They systematically studied the electron emission mechanisms and characteristics of three different tunneling electrodes, namely, tungsten (W), gold (Au), and Platinum (Pt). An optical image and schematic illustration of this air-channel tunneling device are shown in Figure 3b,c, respectively. Due to different work functions and device geometry, the emission in W and Au is fitted with F-N tunneling, whereas the emission is more Schottky-like in the Pt case. Such metal-based tunneling electronic devices provide a platform for future nano vacuum electronics and have the potential to provide a technology basis for low-power, high-performance applications. Nevertheless, it remains difficult for metal-based nanoscale air-channels to be fabricated through

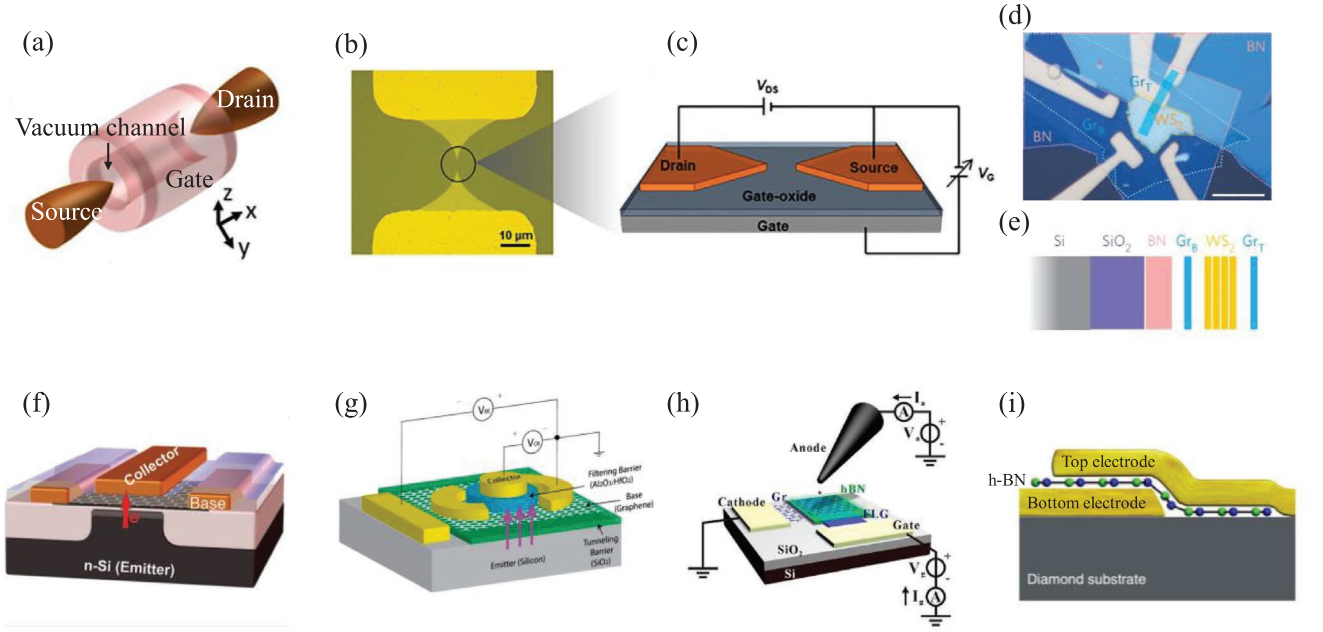

Figure 3. Representative direct tunneling devices. a) Schematic illustrations of a surround-gate electron tunneling device. Reproduced with permission.[16] Copyright 2017, American Chemical Society. b,c) Metal–air–metal tunneling device consist of two in-plan symmetric metal electrodes. b) Top view optical image of fabricated device. c) Schematic illustration of the device structure with a biasing scheme. The metal–air–metal structure depicts drain and source configuration. A dielectric thin film offers separation from conductive back-gate. b,c) Reproduced with permission.[21] Copyright 2018, American Chemical Society. d) Optical image and e) vertical architecture of graphene–WS_2 tunneling transistor. d,e) Reproduced with permission.[90] Copyright 2013, Springer Nature. f) Schematic structure of the graphene-based hot electron tunneling transistor. During device operation, hot carriers are injected from the emitter across the emitter-base insulator and the graphene base into the collector, as indicated by the red arrow. Reproduced with permission.[88] Copyright 2013, American Chemical Society. g) Schematic diagram of the graphene-based hot electron tunneling transistor and the common-base configuration used to measure the I–V characteristics. Graphene is used as the base region for a hot electron transistor structure. The purple arrows indicate the transport direction of the hot electrons. Reproduced with permission.[87] Copyright 2013, American Chemical Society. h) The schematic diagram of the graphene/h-BN hot carrier tunneling device. An anode probe with a voltage of V_a is placed at a distance d above the device. The gate is in a bias of V_g and the cathode is grounded. The anode current I_a and gate current I_g are recorded simultaneously. Reproduced with permission.[91] Copyright 2020, American Chemical Society. i) Simplified side-view illustration of the monolayer h-BN radio-frequency switch based on metal–insulator–metal (MIM) tunneling device. Reproduced with permission.[15] Copyright 2020, Springer Nature.

conventional silicon-foundry-based parallel processes that ultimately support high areal device densities that are manufactured with high production yields. Achieving atomically flat metallic interfaces that retain lattice stability has proven particularly challenging to date.[64–66] Without such ultraprecise surface control, it is believed that further increases in cutoff frequency and power consumption remain limited. This has, in part, driven the search for new materials.

3.1.2. Direct Tunneling Devices Based on Low-Dimensional Nanomaterials

Low-dimensional nanomaterials, and in particular nanocarbon-based materials (such as carbon nanotubes (CNTs) and graphene), have experienced significant interest for their application in electron tunneling applications.[67–71] Their atomic-scale thickness, ability to self-assemble, and unique topologies provide extremely high aspect ratios and thus very high field-enhancement factors that are not attainable by conventional materials and traditional processing either through direct growth or etching. Of the wide range of nanowires discovered and synthesized to date, CNTs have perhaps attracted by far the most attention for use in electron emission systems.[72–74] The electron emission characteristics of a wide variety of CNT types have been studied, including investigations into electric-field driven,[75,76] thermally driven,[54,55] and more recently by strong optical-driven.[72,73] CNTs have been identified as near-ideal field electron emitters. They have, as a result, been widely used in the fabrication of electron tunneling devices over the past two decades. Maruyama and co-workers[77] developed a single CNT tunneling device that demonstrated F-N-like tunneling features.[78,79] This work was successful in demonstrating the potential of such nanomaterials in simplifying nanoscale tunneling channel fabrication, whilst also highlighting the opportunity to capitalize on the self-assembly of nanomaterials to grow nanochannels, en masse in highly parallelized processes that are necessary to realize new device architectures.

As a planar 2D material with single-atom thickness, graphene supports high aspect ratio edge emission. Moreover, it can be structured using more conventional thin film processing techniques, whilst retaining the benefits of its atomic thickness. Extensive theoretical and experimental efforts have demonstrated that graphene can be used effectively in tunneling devices, for both planar[80–84] and vertical structures.[85–91] Mishchenko et al.[90]

reported on a new vertical tunneling FET based on graphene–WS_2 heterostructures, where WS_2 served as an atomically thin barrier between two layers of graphene (Figure 3e). Figure 3d shows an optical image of this device. Capable of achieving an on/off ratio $>10^6$, these devices were shown, for the first time, to operate effectively on optically transparent and mechanically flexible substrates. In addition, vertical graphene-based hot electron tunneling transistors from Lemme et al.[88] have also attracted interest (Figure 3f). When a positive voltage is applied to the graphene base electrode, hot electrons tunnel across the lowered barrier of the emitter-base insulator from the conduction band of the n-doped silicon to the base and adopt F-N-like transport. Similarly, Wang et al.[87] demonstrated a vertical graphene-based hot electron tunneling transistor (Figure 3g) where n-doped silicon, graphene, and aluminum were used as the emitter, base, and collector, respectively. A SiO_2 layer served as the tunneling barrier and an Al_2O_3 layer as the filtering barrier. This graphene-based transistor had high effective gain (4.8%), short transit time (picoseconds), and high current on/off ratio ($>10^5$), suggesting potential applications in future high-speed electronics. Most recently, Chen et al.[91] demonstrated vacuum electron emission under both directions of bias from a vertical Gr/hexagonal boron nitride (h-BN) based heterostructure (Figure 3h), which not only expanded the understanding of hot carrier scattering processes in graphene but also provided important insight into the applications of hot carrier devices.

In addition to graphene, some other 2D materials have also been used in electron tunneling devices to improve their cutoff frequency. Most recently, Akinwande et al.[15] demonstrated that h-BN configured in an MIM on a diamond substrate can be used as an analogue switch for applications in communication systems across radio, 5G and THz frequencies. Figure 3i shows the MIM tunneling structure of a monolayer h-BN radio-frequency switch fabricated on a polycrystalline diamond substrate. These devices showed a low insertion loss (≤0.5 dB), high isolation (up to 200 GHz), and a calculated cutoff frequency of 129 THz due to their nanoscale vertical and lateral dimensions. They offer a low resistance in the on-state and low capacitance in the off-state, metrics that are superior to those of existing solid-state switches. Such MIM-based tunneling devices could lead to the development of nanoscale energy-efficient high-frequency solid-state switch technology for rapidly growing communication systems in the 5G band and beyond.

3.2. Resonant Tunneling Devices

3.2.1. Resonant Devices Based on Traditional Materials

Conventional resonant tunneling devices comprising a quantum well sandwiched between two tunnel barriers that are typically tens of nanometers thick and commonly fabricated from Si/SiGe,[92–94] or III–V quantum well systems.[95–97] Other conventional material systems have also been used.[98,99] Similarly, single-electron tunneling devices have also been realized with various traditional materials, including Si QDs,[100,101] metal nanoparticles,[102,103] single molecules,[104,105] topological insulators,[106] and other more exotic QDs.[107,108] Hiramoto et al.[101] reported on the observation of multiple large quantum-level splitting with extreme charge stability in a Si single-electron transistor (SET) at room temperature. The structure of this device is shown in **Figure 4**a. The device is fabricated from a Si nanowire-channel metal–oxide–semiconductor field-effect transistor, where the Si QD and the tunnel barriers are self-formed by a volumetric undulation process. Recently, Pistolesi et al.[105] theoretically investigated single-photon emission mediated by molecule-based single-electron tunneling devices. Figure 4b shows the schematic of two metallic electrodes forming a plasmonic nanocavity, characterized by a resonance frequency $\omega_c/2\pi$ and a damping rate κ. A single electronic level ε_0 of the molecule in the nanogap couples to the electromagnetic radiation with coupling constant Λ_m. Electrons can tunnel to and from the dot with tunneling rates Γ_α. Nonetheless, so far, despite intensive research efforts exploring a range of different material systems, the obtained performance of the integrated resonant tunneling devices (such as peak-to-valley ratio, response frequency) has been limited.

3.2.2. Resonant Tunneling Devices Based on Low-Dimensional Nanomaterials

Atomically flat interfaces and sharp energy band edges are desirable for the development of tunneling devices.[109,110] 2D van der Waals (vdWs) heterostructures can thus provide unique opportunities for future device design.[111–115] Multilayer stacks of graphene and other atmospherically stable, atomically thin, 2D materials such as boron nitride, the metallic dichalcogenides, MXenes, and layered oxides[116] offer the prospect of the potential creation of a new class of engineered tunneling heterostructure materials. In these structures, different 2D materials and thin insulators can be stacked, often without lattice mismatch and associated band bending constraints, due to the weak vdWs interaction between layers. The increasing availability of numerous different 2D materials—with a variety of different band structures, from semimetals to semiconductors to insulators—makes it possible to assemble entirely unique synthetic materials with engineered band alignments.[109,110,117,118]

The combination of an h-BN barrier layer sandwiched between two graphene electrodes is particularly attractive and has been widely studied during the last decade.[119–122] This has been driven by increasingly improved crystalline quality, excellent transport properties, and the small lattice mismatch, reducing band bending caused by lattice strain, of these two materials. As shown in Figure 4c, Novoselov et al.[121] demonstrated a resonant tunneling graphene-hBN transistor, which employed h-BN as the barrier layer[123] between two graphene electrodes. A tunneling current was generated by the application of a bias voltage, V_b, between the bottom and top graphene electrodes. The gate voltage, V_g, was applied between the doped silicon substrate and the bottom electrode. Resonance occurs when the energy band of the two electrodes are aligned. The tunneling current is exponentially dependent on the h-BN barrier thickness, supporting the speculated quantum transport model. An unprecedented degree of control over the electronic properties is available not only by means of the selection of materials in the stack,[124] but also through the additional fine-tuning achievable by adjusting the built-in strain and relative orientation/rotation of the component layers.[125–129] By aligning the crystallographic orientation of the two graphene

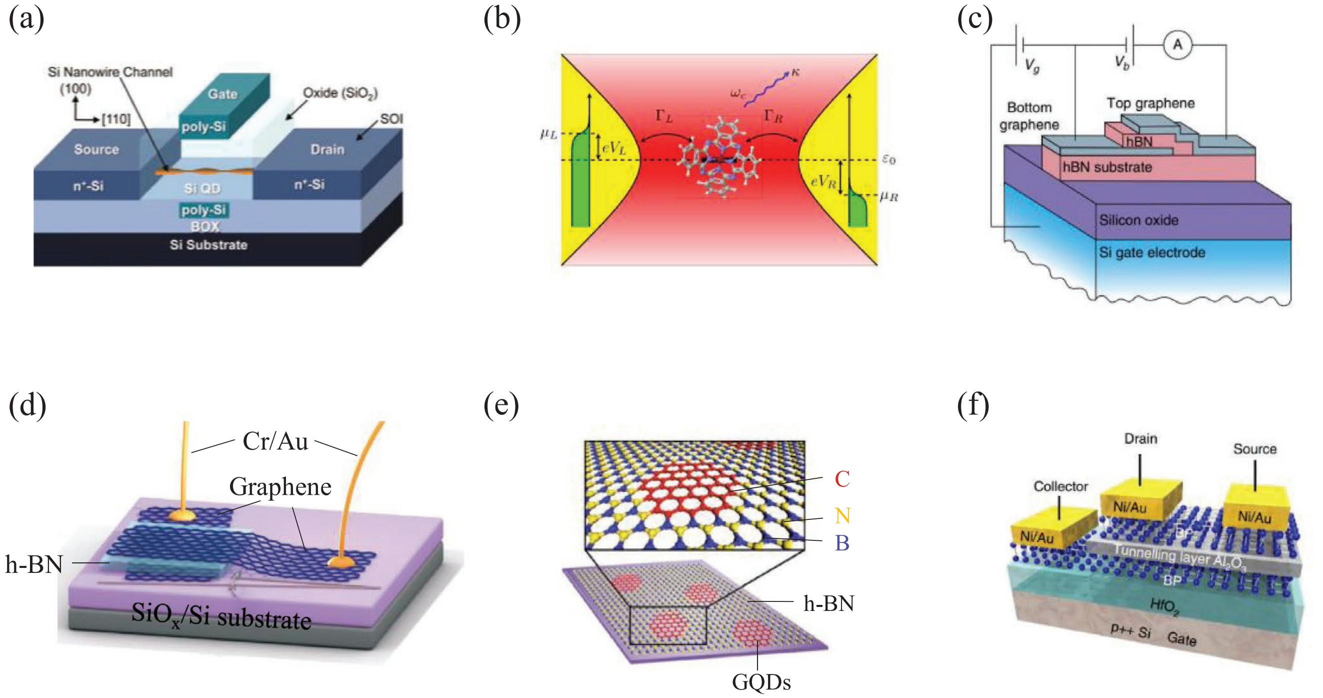

Figure 4. Representative resonant tunneling devices. a) Schematic configuration of the Si-quantum-dot-based single-electron transistor (SET). Reproduced with permission.[101] Copyright 2014, American Chemical Society. b) Schematic of a typical molecule-based SET. Two metallic electrodes forming a plasmonic nanocavity characterized by a resonance frequency $\omega_c/2\pi$ and damping rate κ. Electrons can tunnel to and from the dot at tunneling rates Γ_α. Voltage drops, V_α, with respect to ε_0 are indicated. Reproduced with permission.[105] Copyright 2019, American Physical Society. c) Schematic diagram of the graphene-BN resonant tunneling transistor. Reproduced with permission.[121] Copyright 2013, Springer Nature. d) Device schematics of the resonant tunneling transistor with an exaggerated angle θ between two graphene layers (separated by an h-BN tunnel barrier shown in light blue). Both graphene layers are independently contacted by Cr/Au metallization (yellow). Reproduced with permission.[122] Copyright 2014, Springer Nature. e) Schematic of the in-plane SET based on graphene-quantum-dots (GQDs). Reproduced with permission.[130] Copyright 2019, Springer Nature. f) Schematic view of the vertical van der Waals structure based on BP/alumina/BP. Reproduced with permission.[131] Copyright 2020, Springer Nature.

layers in the graphene/h-BN/graphene heterostructure, the same team demonstrated that this device can achieve resonant tunneling with conservation of electron energy, momentum, and, potentially, chirality.[122] Figure 4d depicts the schematic of this resonant tunneling transistor with an exaggerated angle θ between two graphene layers (separated by an h-BN tunnel barrier shown in light blue). The heterostructure is placed on a SiO$_x$/Si substrate (magenta/light gray), which serves as an electrostatic gate. These resonant tunneling devices are free of the fundamental limitation intrinsic to conventional double-barrier resonant tunneling devices, namely the relatively long carrier dwell time (picoseconds) in the quantum well as compared with the time to transit the barrier (femtoseconds). Therefore, such tunnel circuits have extraordinary potential in shaping future high-speed electronic devices.

Most recently, Kim et al.[130] demonstrated the simultaneous use of planar graphene-based vdWs heterostructures to build vertical SETs. As shown in Figure 4e, graphene QDs are grown inside a matrix of h-BN, which dramatically reduces the number of localized states along the perimeter of the QDs. The use of h-BN tunnel barriers as contacts to the graphene QDs make SETs reproducible and independent of localized states, which open up many opportunities in the design of future devices.

Other layered nanomaterials are also used in resonant tunneling devices. Most recently, Wu et al.[131] reported a tunneling field-effect transistor made from a black phosphorus (BP)/Al$_2$O$_3$/BP vdWs heterostructure in which the tunneling current was in the transverse direction with respect to the drive current. A schematic of the device is shown in Figure 4f. The top BP layer is p-doped while the bottom BP layer is n-doped. There is a remarkable NDR behavior, showing an abrupt decrease in drain current for a small change in drain voltage. In this NDR region, the drain current is more than 10^3 times larger than the gate leakage current I_g or collector current I_c. This is fundamentally different from conventional tunneling devices where the tunneling current typically equals the change in drain current. Through an electrostatic effect, this tunneling current can induce a dramatic change in the output current, leading to a tunable NDR with a peak-to-valley ratio > 100 at room temperature.

With continued research into new 2D materials and new vdWs heterostructures, it is becoming more widely accepted that a variety of new and important tunneling applications have and will continue to emerge, including novel photodetectors,[97] evaporative electron cooling,[132] and resonant tunneling spectroscopy,[133] all of which serve to further highlight the continuing technological value and importance of new resonant tunneling devices.

3.3. Inelastic Tunneling Devices

In this section, we focus on photon and gap plasmon emission; a specific case of inelastic tunneling. One of the most attractive applications of inelastic tunneling devices perhaps lies in the realization of nanoscale light sources. Inelastic electrically excited spontaneous radiation through a tunnel junction was first observed in an MIM structure in 1976 by Lambe and McCarthy.[134] This emission is a two-step process. A gap plasmon is first excited in the MIM junction. This gap plasmon leads to light emission by either decaying directly into a photon or by coupling to a surface plasmon.[51,135,136] Such optical sources can confine light to the nanoscale through interface resonance effects.[137] Generally, the low generation ratio of inelastic electrons restricts the electron-to-plasmon conversion efficiency (<10%). The plasmon-to-photon conversion efficiency is also similarly extremely low (<0.1%) due to wave-vector mismatch.[41] These adverse factors lead to comparatively low light emission efficiency (10^{-3}–10^{-2}%) that make practical applications of such nanoscale light sources difficult.[42] Nevertheless, local optical hot spots introduced by surface plasmon resonances have been shown to enhance the electron-to-photon conversion efficiency by a factor of 10^2, resulting in potentially functionally viable light emission efficiencies of around 2%.[42,138,139] Tunneling junctions with integrated optical antennas efficiently bridge the size mismatch between nanoscale volumes and far-field radiation and in doing so are one approach toward dramatically enhancing the electron–photon conversion efficiency. Electron tunneling structures have been shown to support electric-field-driven light generation via inelastic tunneling in metal–insulator–semiconductor[140,141] and MIM[41–43] tunneling junctions, with much on-going research exploring the use of these structures in more advanced architectures.

3.3.1. *Inelastic Tunneling Devices Based on Traditional Materials*

An electric-field-driven optical antenna was first demonstrated by Hecht et al.[43] in 2015. An electron micrograph of this lateral tunneling structure is shown in **Figure 5**a. Subsequent to this, Novotny et al.[41] demonstrated an antenna-coupled MIM tunneling junction, as shown in Figure 5b. These tunneling

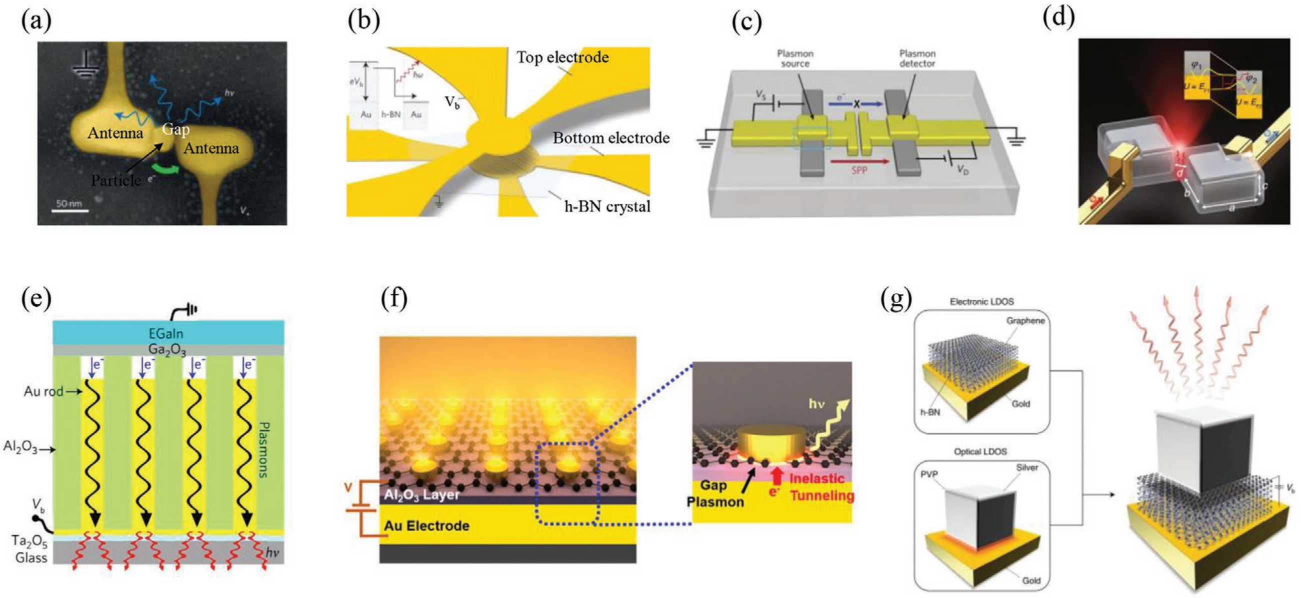

Figure 5. Representative inelastic tunneling devices. a) Electron micrograph of a lateral tunneling device: an electrically connected single-crystalline gold nanoantenna loaded with a coated gold nanoparticle on a glass substrate. *V*+, applied voltage; *e*–, electron flow; *hν*, light emission. Reproduced with permission.[43] Copyright 2015, Springer Nature. b) Schematic illustration of metal–insulator–metal (MIM) tunneling devices. The devices consist of a vertical stack of segmented, nanostructured Au bottom electrodes, few-layer h-BN, and a common Au top electrode. Inset: Generation of a photon with energy $\hbar\omega$ by inelastic electron tunneling. Reproduced with permission.[41] Copyright 2015, Springer Nature. c) Schematic illustration of a device consisting of two MIM tunneling junctions connected to a plasmonic waveguide. The left junction is the plasmon source and the right junction is the plasmon detector. Reproduced with permission.[44] Copyright 2017, Springer Nature. d) Schematic diagram of a tunnel junction formed by two edge-to-edge Ag single-crystal cuboids encapsulated by a layer of polymer. The top inset shows that the photons are generated through inelastic electron tunneling. Here, E_{F1} and E_{F2} are the Fermi energies of the left and right Ag cubes, respectively. The device performance can be engineered by tuning the geometrical parameters of the tunnel junction including the gap size *d*, the size of the cuboids (*a, b, c*), and the curvature of the Ag cuboid edges. Reproduced with permission.[42] Copyright 2018, Springer Nature. e) Schematic of the configuration of an electrically driven nanorod metamaterial based on metal–air–metal tunnel junctions. When a bias is applied between the EGaIn layer and Au nanorods, electrons tunnel across the junctions from occupied states in EGaIn to unoccupied states in Au. Reproduced with permission.[45] Copyright 2018, Springer Nature. f) Schematic image of light emission from a nanoparticle array using a graphene tunnel junction (left) and underlying emission mechanism (right). A single plasmonic nanoparticle generates light when a voltage is applied across the tunnel barrier. The tunneling electrons lose their energy by exciting gap plasmons of the single nanoparticle and the exciting gap plasmons decay into far-field radiation. Reproduced with permission.[49] Copyright 2018, American Chemical Society. g) Illustration of a gold-few-layer h-BN-graphene van der Waals quantum tunneling (vdWQT) device, integrated with a (silver, PVP-coated) nanocube antenna. In this device configuration, the electronic LDOS is controlled by the hybrid vdWs heterostructure whereas the optical LDOS is governed by the nanocube antenna. Applying a voltage V_b across the insulating few-layer h-BN crystal results in antenna-mediated photon emission (wavy arrows) due to quantum tunneling. Reproduced with permission.[50] Copyright 2019, Springer Nature.

junctions consisted of a vertical stack of segmented, nanostructured Au bottom electrodes, few-layer h-BN and a common Au top electrode. The emission originates from inelastic electron tunneling in which the energy is transferred to surface plasmon polaritons (SPPs) and subsequently converted to far-field radiation by an optical antenna (inset of Figure 5b). It was found that the spectrum of the emitted photons was determined by the antenna geometry and can be readily tuned via the application of a voltage to the antenna. It was observed that the direction and polarization of the light emission can be controlled by engineering the antenna resonance, which has the added benefit of improving the external quantum efficiency by approximately two orders of magnitude.[43] Nijhuis et al.[44] demonstrated an MIM tunneling junction in an on-chip electronic-plasmonic transducer with an effective efficiency of ≈14%. This ultracompact device integrated light emission and detection on a single chip. Figure 5c shows how the two MIM tunneling junctions are plasmonically coupled via their Au leads, which serve as the plasmonic waveguide. Later, Liu et al.[42] reported on a Ag nanoantenna tunnel junction with a large local density of optical states (LDOS) in the tunneling nanogap. This structure was shown to increase the far-field light emission efficiency from ≈0.01% to ≈2%. This inelastic tunneling device is schematically illustrated in Figure 5d. Here, photons are emitted from an electronically biased junction formed by two Ag nanocrystals. Such inelastic electron tunneling devices have significant potential in the ultrafast conversion of electrical signals to optical signals at the nanoscale, which can be used in integrated electric-field-driven light sources with controlled emission frequencies for potentially technologically disruptive high-speed on-chip interconnection applications.

Recently, inelastic electron tunneling devices were explored for new applications in chemical catalysis.[45] Figure 5e shows the device configuration of electrically driven plasmonic nanorod metamaterials based on metal–air–metal tunneling junctions using liquid eutectic gallium indium (EGaIn) as a top contact. The majority of the electrons tunnel elastically to form hot electrons in the Au nanorod tips; the inelastically tunneling electrons excite surface plasmons in the metamaterial, which then decay nonradiatively via the excitation of hot carriers or radiatively into photons from the substrate side of the metamaterial. By monitoring either the changes in the tunneling current or the light intensity due to radiation of the excited plasmonic modes, the reactive tunnel junctions have the potential to control chemical reactions at the nanoscale.

3.3.2. Inelastic Tunneling Devices Based on Low-Dimensional Nanomaterials

Besides metal-based tunneling structures, a variety of novel nanocarbon materials have been used in a range of inelastic tunneling devices. Graphene-based inelastic tunneling devices have shown considerable promise due to the linear dispersion of their Dirac cone, a tunable Fermi level, and nearly flat absorption profile.[142–144] Koester et al.[49] reported on an ultrasmall (<100 nm) plasmonic single nanoparticle light source driven by a graphene tunneling junction. A schematic of the device structure and the light emission mechanism is shown in Figure 5f. A gap plasmon is formed between a base Au electrode and a single Au nanoparticle separated by a thin (<10 nm) dielectric gap. This gap mode is electrically excited by electrons inelastically tunneling from the base electrode, through a thin Al_2O_3 dielectric, and into a graphene layer located underneath the nanoparticle. Graphene acts as an ultrathin transparent counter electrode for tunneling while minimizing disruption of the plasmon mode. Novotny et al.[50] demonstrated light emission from van der Waals quantum tunneling (vdWQT) devices. These devices comprise a vertical stack of Ag, h-BN, and graphene, as illustrated in Figure 5g. Applying a voltage V_b across the insulating few-layer h-BN crystal results in antenna-mediated photon emission. Photon emission from inelastic electron tunneling can be locally enhanced by coupling to an optical antenna. This can achieve resonant enhancement of the photon emission rate in narrow frequency bands (full width at half maximum of ≈57 meV) by four orders of magnitude. Nanocube antennas provide a high local density of states (LDOS) and give rise to a narrow emission spectrum. In this device configuration, the electronic LDOS is controlled by the hybrid vdWs heterostructure whereas the optical LDOS is governed by the nanocube antenna. The optical mode confinement in these vdWQT devices can be defined independently of the electrical tunnel junction—establishing a new paradigm in nanoscale optoelectronic interfacing.

Advances in nanocarbon-based science during the last decade have driven a recent explosion of new materials that provide an unprecedented variety of novel transport mechanisms which has served to accelerate research in the tunneling devices community. Clearly, direct tunneling devices have demonstrated far-reaching potential as the physical basis for achieving high-speed electronic devices in a variety of technologies. Much work, however, remains to be undertaken to improve the existing devices and to develop new concepts for devices with radically enhanced efficiency and speed.

4. Optical-Field-Driven Electron Tunneling Devices

The time that it takes for electrons to directly tunnel through a barrier with nanoscale thickness has been intensely discussed in the literature.[145–148] In 2018, Gabelli et al.[149] demonstrated that the tunneling time in electrically driven metallic tunneling junction by quantum shot noise is as fast as 1 fs. The development and use of ultrashort pulsed lasers to excite electron tunneling across nanogaps has, since then, been shown to further set upper limits for the tunneling time of the order of attoseconds.[3,4,6,7] This, in principle, will enable optical-field-driven electron tunneling devices to operate at sub-optical-cycle timescale.[150] The following section presents recent advances in optical-field-driven tunneling devices, focusing on the novel tunneling phenomenon based on different mechanisms.

4.1. Optical-Field-Driven Direct Tunneling Devices

At present, the development of ultrafast optical-field-driven electron tunneling devices is still at the proof of principle stage.

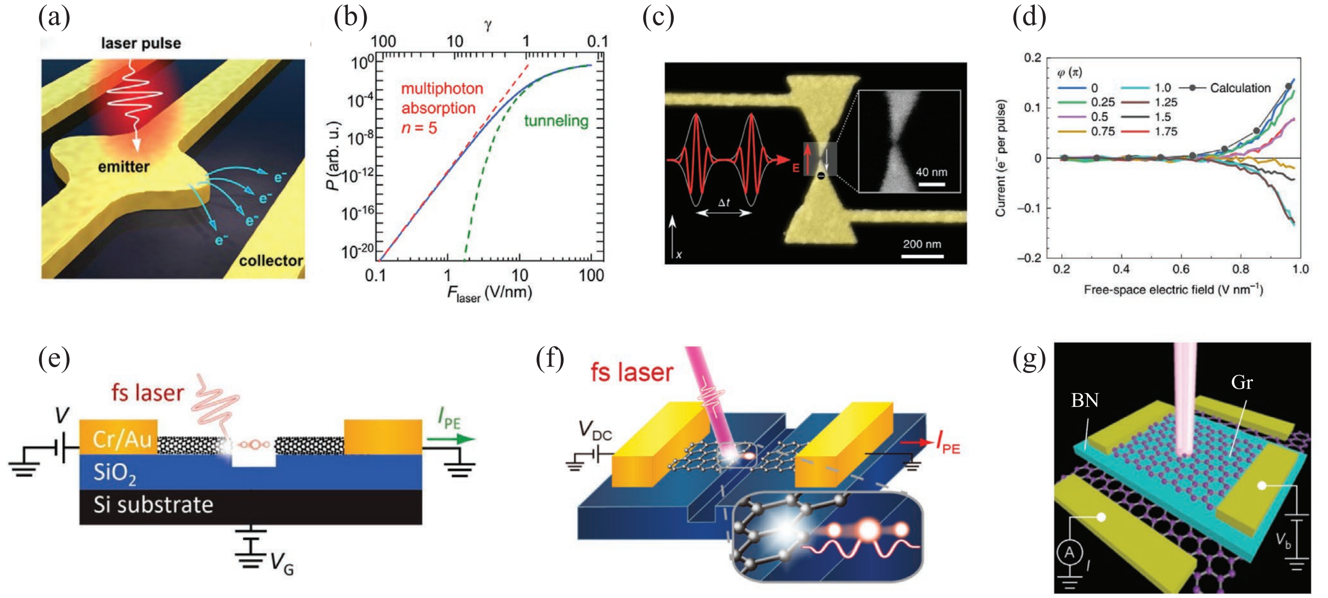

Figure 6. Representative optical-field-driven direct tunneling devices. a) Sketch of a metallic tunneling junction with electrons being emitted after excitation with a femtosecond laser pulse (Laser energy: 0.9–1.3 eV, F_{laser}: 0.6 V nm^{-1}). b) Electron emission probability as a function of the lasers optical field intensity F_{laser} as suggested by Keldysh Theory (blue line). The corresponding Keldysh parameter γ is displayed on the top axis. For a low F_{laser}, the Keldysh curve approaches the multiphoton absorption regime (red dashed line), whilst for a high F_{laser}, the Keldysh curve is approximated by an optical-field tunneling probability (green dashed line). a,b) Reproduced with permission.[158] Copyright 2019, American Chemical Society. c) SEM image of a gold bow-tie antenna with two electric contacts. Two single-cycle laser pulses delayed by a time Δt are focused onto the nanogap. The red arrow indicates the positive direction of the electric field and the white arrow gives the corresponding direction of the electron transfer. Inset: Enlarged view of the gap region. d) The pulse-averaged light-driven current induced as a function of free-space electric field amplitude of the laser pulses. The current is modulated sinusoidally with a phase φ that is directly related to the far-field CEP of the driving pulse φ = CEP+δ. c,d) Reproduced with permission.[154] Copyright 2019, Springer Nature. e) Schematic of femtosecond-laser-induced field emission in the SWNT nanogap device. Reproduced with permission.[165] Copyright 2019, AIP Publishing. f) Schematic of femtosecond-laser-induced field emission in a graphene nanogap tunneling device. Reproduced with permission.[166] Copyright 2018, American Chemical Society. g) Schematic of a Gr-BN-Gr device under optical excitation. Reproduced with permission.[167] Copyright 2016, Springer Nature.

Though at a low technology readiness level, advances in materials science, coupled with access to novel fabrication processes and new excitation methodologies are helping to accelerate the technology development in this area toward an exciting optoelectronic integrated future. The present state-of-the-art is seeing researchers use ultrafast lasers to excite different asymmetric structures, allowing for the exploration of a range of exotic ultrafast electron emission processes in tunneling structures, some of which are explored here.

4.1.1. Devices Based on Traditional Materials

Antenna coupled nanojunctions have attracted much attention due to their extremely high field-enhancement. Amongst the metallic nanoantenna structures, bow-ties have been widely used in high-harmonic generation,[151,152] optical rectification,[150] attosecond electronics,[153,154] and terahertz switching.[155,156] Similarly, bow-tie-related structures have been used in optical-field-driven electron tunneling devices to achieve high field-enhancement, briefly described in the following.

To combine the advantages of ultrafast femtosecond nano-optics with an on-chip communication scheme, optical signals with a frequency of several hundreds of THz need to be downconverted to coherent electronic signals capable of propagating on-chip. For this purpose, Holleitner et al.[157] exploited femtosecond photoswitches based on asymmetric metallic nanogap junctions. They demonstrated that 14 fs optical pulses in the near-infrared can drive electronic circuits with a prospective bandwidth of up to 10 THz. More recently, the same team demonstrated a unipolar ballistic electron current with an asymmetric metallic nanogap junction, which might be used for molecular electronics or as ultrafast photoswitches for THz electronics.[158] **Figure 6**a shows the photoemission process of an asymmetric metal nanogap excited by an ultrafast laser pulse. As the laser field is plasmonically enhanced by the geometry's asymmetry, electrons are emitted from the emitter electrode into the gap and then to the collector electrode. The nonlinear photoemission processes associated with this transport are shown in Figure 6b. When the peak electric field amplitude of the laser, F_{laser}, is low ($\gamma \geq 1$), the emission current is dominated by multiphoton absorption (dashed red line in Figure 6b),[60] and the power-law coefficient is similar to the number of absorbed photons.[59] The electron emission can be described by the optical-field tunneling process (dashed green line in Figure 6b) when F_{laser} is high (>10 V nm^{-1}).[61]

Understanding the optical-field-driven electron dynamic in tunneling junctions has been found to be crucial in the design of integrated plasmonic and optoelectronic devices that operate at attosecond timescale. Brida et al.[153] reported a coherent control of the electron tunneling control in a bow-tie structure using the CEP of a short-pulse laser. Due to the high field enhancement in the gap region (≈35), the peak current densities of the device were very large (50 MA cm^{-2}) and corresponded to the transfer of individual electrons in a half-cycle period of 2 fs. More recently, the same team measured interferometric autocorrelations of an ultrafast current induced by optical field emission across a nanogap consisting of a single plasmonic nanocircuit. It was shown that the measured response reflects the interplay between the CEP of the driving pulse, the plasmonic resonance of the antenna, and quiver motion of the released electron.[154] Figure 6c depicts the conceptual scheme of this experiment. The single-cycle pulses were set to variable time delays Δt and then focused tightly onto a single plasmonic bow-tie antenna. The relative CEP of the biasing pulses could be fully controlled with a precision of 10 mrad. The Au nanoantenna features a 6 nm gap (inset of Figure 6c). Under a static time-invariant electric bias, this structure exhibits an I–V characteristic that is antisymmetric and highly nonlinear.[153] As a result, an optically induced symmetry breaking occurs which leads to a net current that depends on the CEP of the driving pulse. Consequently, for a 2π CEP sweep, the integral current passes through a maximum, crosses zero, and finally completely reverses its direction. The current measured as a function of the optical field amplitude of the single-cycle pulses is shown in Figure 6d. The current is modulated sinusoidally with a phase of φ that is directly related to the far-field CEP of the driving pulse ϕ = CEP + δ. Understanding such optically driven electron dynamics at the nanoscale will facilitate control over electron transport on atomic time and length scales, which promises unprecedented precision and control for new devices, such as CEP photodetectors or ultrafast all-optical transistors and gates.

4.1.2. Devices Based on Low-Dimensional Nanomaterials

Nanocarbon materials have the potential to serve as an ideal material platform for the electron tunneling devices working in the optical-field-driven regime.[72–74] Optical rectenna can directly convert free-propagating electromagnetic waves at optical frequencies to direct current.[159] The cutoff frequency for a rectenna is defined as $f_c = 1/(2\pi R_A C_D)$,[160] where R_A is the antenna resistance and C_D is the capacitance of the rectenna diode. The diode capacitance is given by $C_D = \varepsilon_0\,\varepsilon A/d$, where ε_0 is the permittivity of vacuum, ε is the relative permittivity of the insulator, A is the area, and d is the insulator thickness. Diodes operating at cutoff frequencies on the order of 1 PHz (switching speed ≈1 fs) are feasible if their capacitance is on the order of a few attofarads (aF).[160,161] This can be realized by a suitably designed antenna coupled to a diode. Cola et al.[162] demonstrated an optical rectenna operating at 564 THz by engineering an MIM tunnel diode, with a junction capacitance of ≈2 aF, at the tip of a vertically aligned multiwalled CNT (≈10 nm in diameter), which acted as the antenna.[163,164] Due to self-assembly, nanocarbon-based devices are significantly easier to fabricate at the nanoscale than traditional materials-based devices, improving not only device yield but also the device optical cutoff frequency.

Recently, electronic control of an ultrafast tunneling electron emission source was demonstrated in a single-walled CNT (SWNT) nanogap irradiated by a femtosecond laser pulse,[165] as schematically illustrated in Figure 6e. The photoinduced field emission in this SWNT device exhibited switching operation due to gate-induced variations in the effective barrier height. The photoelectron emission was tuned by gate-induced changes in the electronic band structures. As a result, the use of an SWNT provided an additional degree of freedom for controlling the electron emission yield and dynamic electron motion in the strong-field tunneling regime. Since then, nonlinear strong-field photoemission has recently been reported for a semiconducting SWNT emitter,[165] which may prove particularly useful for future applications in attosecond electronics and photonics.

The atomically sharp edges and large crystallographic damage of the family of graphitic nanocarbons, and in particular graphene, are of key importance for their impressive ultrafast electron emission properties, specifically in the strong-field tunneling regime.[166] As schematically illustrated in Figure 6f, strong photoinduced currents were produced when the gap area was irradiated by a focused ultrashort pulse laser (wavelength, $\lambda = 800$ nm). Optical-field emission dominates the emission process for $\gamma \leq 1$, whereas γ has been limited to ≈0.7 for $\lambda < 1$ µm. The graphene-based tunneling device achieved $\gamma < 0.5$ for an extremely low laser pulse energy of 15 pJ, owing to the large field enhancement of these 2D materials. At the maximum power condition, an extremely low Keldysh parameter of $\gamma = 0.2$ can be reached.[166] For the low-power condition, most of the photoemitted electrons undergo a quiver-motion and as a result, the electron wavepacket extends in time over an interval of the order of 10 fs. Conversely, in the high-power regime, more electrons are emitted in the sub-cycle, traversing the optical near-field of the antenna within less than one half cycle. This results in considerably shorter wavepackets than in the low-power case. A notable transition in the dynamic behavior of the electron emission can therefore be achieved by going from quiver motion to the sub-cycle motion with a change in the field intensity of the driving pulse. This result indicates that strong-field emission will allow for the creation of trains of ultrafast electron wavepackets with a temporal width of less than one half-cycle of the incident laser pulses. Ma et al.[167] demonstrated the control of ultrafast electron thermalization in a graphene–hBN–graphene structure (Figure 6g), which showed a transition between different tunneling regimes and offered a means to modulate the electron energy transport in ultrafast tunneling dynamics. Some other low-dimensional nanomaterials, such as transition metal dichalcogenide (TMD), are also explored in optical-field-driven tunneling devices due to their optoelectronic properties.[168] Sushko et al.[169] reported large photocurrents upon optical excitation in h-BN/TMDs devices, which is attributed by Auger recombination in the TMDs. The primary difficulty in utilizing nanocarbon-based materials lies in their large-scale uniform preparation; however, steady progress continues to be made and such materials are viewed as being increasingly practical for deployment by many. In the near term, nanocarbon-based nanogaps will continue to be used to make important contributions to the development of tunable devices that can produce ultrashort electron pulses for future applications in table-top attosecond streaking, spatiotemporal imaging and high-speed electronics.

Most recently, using semiconducting CNT emitters, Dai et al.[73] demonstrated an extreme nonlinear photoemission

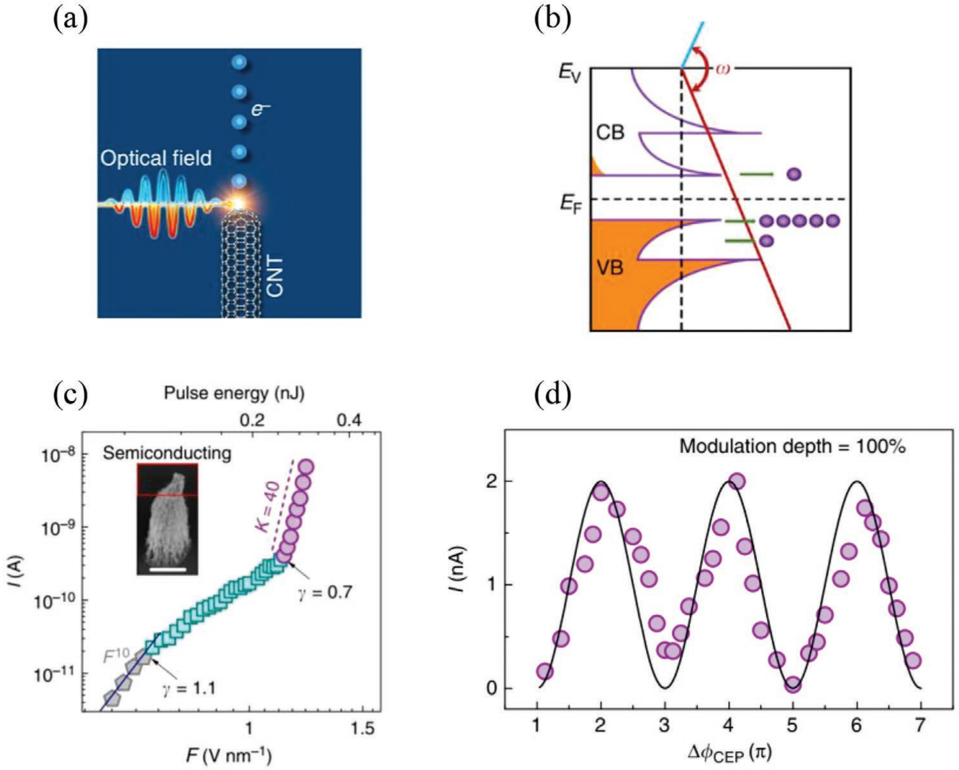

Figure 7. Extreme nonlinear strong-field photoemission from CNTs. a) Diagram of optical-field emission (OFE) from CNT. Electrons (blue balls) are emitted from semiconducting CNT, driven by a negative half-cycled (red line) strong electromagnetic field of a femtosecond laser. b) Diagram of transition into the valence band-dominated OFE (VB-OFE) that occurs at a relatively high optical-field strength. c) *I*–*F* curve of aged CNT cluster in which the metallic tubes have been removed. Three different regimes of nonlinear behavior are observed: multiphoton photoemission (MPP) (gray pentagonal dots); conduction band-dominated OFE (CB-OFE) (green square dots); VB-OFE (purple circular dots). An extremely high slope of $K = 40$ (dashed line) was observed. The inset shows the SEM image of the emitter. Scale bar is 2 µm. d) The CEP-dependent photoemission current at a fixed laser intensity with a peak $F = 1.3$ V nm^{-1} together with a cosine fit (solid line). a–d) Reproduced with permission.[73] Copyright 2019, Springer Nature.

behavior in the strong-field regime.[72,170] In the case of 1D CNTs (**Figure 7**a), electron tunneling may start from CB states at a relatively low field due to the lower barrier height. However, the electron density in the edge of the valence band (VB) is much higher than that in the CB states. As a result, the emission current from the VB edge can be comparable to or even larger than that from the CB (Figure 7b). Figure 7c shows the measured optical-field (*F*) dependent total photoemission current (*I*) for this CNT emitter. The *I*–*F* curve reveals a conventional strong-field photoemission behavior in the low-field section, with a transition the multiphoton photoemission (MPP) (gray pentagonal dots, Figure 7c) to an OFE regime (CB-OFE, green square, Figure 7c). At $F \approx 1.1$ V nm^{-1} (corresponding to $\gamma \approx 0.7$), an extremely nonlinear strong-field photoemission curve with a curve slope of up to 40 can be achieved and a new emission regime sets in which is termed the VB-OFE regime (purple circular, Figure 7c). As shown in Figure 7d, in the VB-OFE regime, *I* is modulated effectively with a depth up to 100% by changing the CEP. This result clearly shows that full access to the VB-OFE regime can offer more sensitive-CEP-control over the photoemission process than previously achieved. This is promising for the development of sensitive CEP detectors simply by using a source meter.[3]

The high spatial and temporal resolution, high modulation sensitivity, control over the electron motion, and sub-optical-cycle response of direct tunneling electronic devices ensure that such devices present unprecedented potential in nonlinear optics, femtosecond and even attosecond optoelectronics.

4.2. Optical-Field-Driven Resonant Tunneling Devices

Recently, the optical-field-driven method has been extended to other electron tunneling mechanisms, such as resonant tunneling[171] and inelastic tunneling.[172] Davidovich[171] demonstrated a new model of time-dependent tunneling without the introduction of boundary conditions. Here they propose a joint solution of the time-dependent Schrödinger and Poisson equations, which is used to analyze the optical-field-driven double-barrier resonant tunneling diode. The model is based on an integral equation obtained by the time-dependent Green's function method. The potential function profile of a two-barrier structure is shown in **Figure 8**a, which depends on the doping profile and barrier widths. Figure 8b shows the calculated voltage *U* (1, right scale) and current density *J* (2, left scale) as a function of dimensionless time. A phase shift of approximately π is seen in Figure 8b, which indicates that the differential conductivity is negative and the structure can serve as a generator of ω_0 and $3\omega_0$ frequencies. This new model of

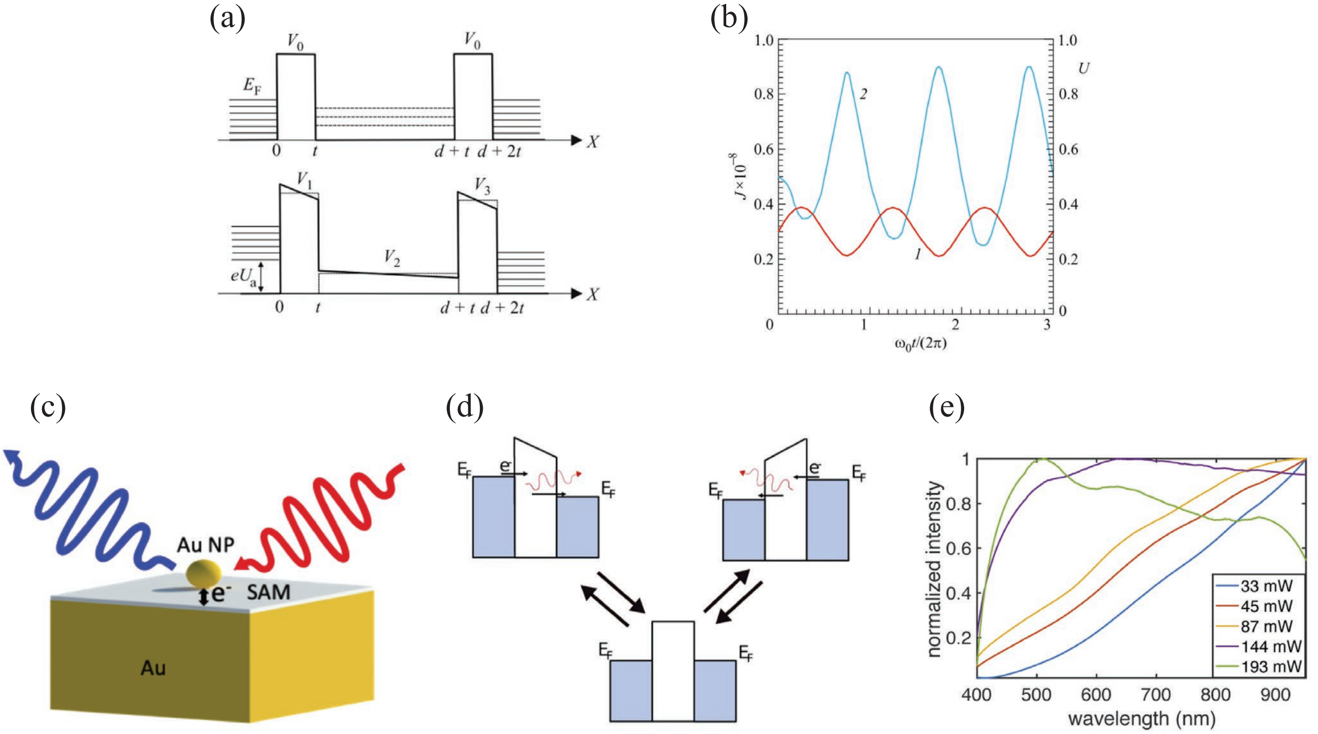

Figure 8. Other novel optical-field-driven tunneling devices. a,b) Time-dependent resonant tunneling in a double-barrier diode structure. a) Top: potential function profile for the symmetric double-barrier structure (the energy is measured from the bottom of the conduction band of the cathode). Bottom: Its distortion induced by the voltage U_a applied to the anode (the energy is measured from the bottom of the conduction band of the anode). b) Voltage U and current density J versus the dimensionless time $\tilde{t} = \omega_0\, t/(2\pi)$. a,b) Reproduced with permission.[171] Copyright 2019, Springer Nature. c–e) Light-induced inelastic tunneling emission. c) Schematic of a metal nanoparticle on an ultraflat gold film covered with a self-assembled monolayer. An incident light pulse drives electron tunneling which emits a higher energy photon due to inelastic scattering. d) Schematic of light-induced inelastic tunneling emission (LITE) effect resulting from the AC field of a femtosecond laser creasing an oscillating bias voltage across the tunnel junction. The bias field is represented by a slope in the barrier potential. When the field induces tunneling, an upconverted photon can be emitted by inelastic scattering. e) Emission spectra for four different average powers, showing the characteristic spectral shift of LITE. c–e) Reproduced with permission.[172] Copyright 2020, Optical Society of America.

time-dependent tunneling has been proposed to describe time-dependent resonant tunneling diodes and other structures with several barriers varying in time in a finite region, and can concurrently, be used to solve the open problem of the wavepacket tunneling time.[173]

4.3. Optical-Field-Driven Inelastic Tunneling Devices

Gordon et al.[172] first demonstrated light-induced inelastic tunneling emission (LITE) in metal tunnel junctions. This device is shown schematically in Figure 8c. Similar to electric-field-driven inelastic tunneling device, it can produce photon emission. Figure 8d shows a schematic of this effect where the energy gap of a nanoscale self-assembled monolayer presents a tunneling barrier and the energy bias across the barrier oscillates with the applied field from the femtosecond pulse. Figure 8e shows the LITE spectra recorded on a fiber-coupled photon-counting spectrometer. The extremely bright emission from the LITE process can be observed by the naked eye. This phenomenon is promising for producing ultrafast upconverted light emission with higher efficiency than conventional nonlinear processes. By exploiting plasmonic resonances, the reduced tunneling bandwidth and more stable junction materials, LITE has significant potential for the realization of a highly efficient ultrafast source of upconverted photons.

Recent studies of optical-field-driven electron tunneling devices have already demonstrated great potential in achieving high working frequencies and in doing so have revealed a plethora of new and enticing physics in field-driven electron dynamics. Though moving rapidly, further theoretical and experimental research is crucially needed. For example, in the direct tunneling regime, transport in optical-field-driven electron dynamics in nanogap is not clear yet, in part due to the large parameter space which includes size and electronic structure of the nanoscale emitting tip, and the laser wavelength and intensity. Also, up to date, most of the work has focused on controlling electron dynamics optical-field emission in new types of tunneling devices. So far, only few studies have analyzed the interaction of the tunneling electrons with solid-state quantum emitters. Such experiments are of crucial relevance for exploiting the enormous potential of tunneling devices in future ultrafast all-optical and quantum optical information processing.

5. Outlook

Primary studies have demonstrated that optically controlled electron tunneling through nanojunctions and nanogaps may, in principle, greatly increase the speed of future electronic devices by five to six orders of magnitude, providing unprecedented access to an entirely new class of electronics that are cable of operating at Peta-hertz (10^{-15} Hz) frequencies. The atomic-scale tunneling emission surfaces of newly emerging low-dimensional materials, such as carbon nanomaterials, are proving to be key in the development of new approaches to sub-femtosecond duration tunneling; and in doing so will play a key role in achieving Peta-hertz devices. However, before achieving such a landmark achievement a number of major fundamental and technical challenges must be addressed. For instance, the fundamental physics of the process of optical-field-driven electron tunneling in low-dimensional nanoscale systems must be distinctive due to the quantized electronic structure, compared to traditional materials with continuous electronic structure. This should be further elucidated, with ongoing investigations into strongly coupled ultrafast dynamics such as electron–electron, electron–phonon, and electron–plasmon interactions, all of which are likely to require parameter decoupling through the use of extreme conditions including cryogenic temperatures and ultrashort laser pulses. Concurrent time-dependent ab initio calculations will prove essential in the design of materials and device architectures. With a focus on materials, highly stable strong-field photoemission materials, with unique properties such as low work function, high breakdown threshold, controllable and engineered doping profiles and band structures, designed by density functional theory and synthesized by atomic-precision additive-manufacturing will be an essential element of the emerging "lightwave electronics" toolbox. Most importantly, increasing studies of the interaction of tunneling electrons with quantum emitters are needed to devise new classes of all-optical and quantum optical switching devices. Such work offers the exciting prospect of merging some of the recent developments in ultrafast electron microscopy and tunneling devices, potentially providing a new level of control over the dynamics of electrons in functional nanodevices. With continued convergence of strong-field physics, attosecond technology, and materials science, optical-field-driven electron tunneling devices working at attosecond timescale are looking to be increasingly attainable. Based on optical-field-driven electron tunneling, such systems will drive a new paradigm in high-speed optoelectronics and in doing so will reshape modern information technology.

Acknowledgements

The authors acknowledge funding from the National Key R&D Program of China (Grant No. 2016YFA0202000), the National Natural Science Foundation of China (Grant Nos. 51972072, 52072084, 51925203 and 91833303), the Key Research Program of the Chinese Academy of Sciences (Grant No. ZDBS-SSW-JSC002), CAS Interdisciplinary Innovation Team (Grant No. JCTD-2018-03), the Strategic Priority Research Program of the Chinese Academy of Sciences (Grant Nos. XDB36000000), and the Priority program QUTIF of the Deutsche Forschungsgemeinschaft (SPP1840).

Conflict of Interest

The authors declare no conflict of interest.

Keywords

direct tunneling, electron tunneling devices, inelastic tunneling, optical-field-driven, resonant tunneling, single-electron tunneling

Received: February 20, 2021
Revised: April 5, 2021

[1] R. H. Dennard, F. H. Gaensslen, H. N. Yu, V. L. Rideout, E. Bassous, A. R. Leblanc, *IEEE J. Solid-State Circuits* **1974**, *Sc 9*, 256.
[2] E. Goulielmakis, V. S. Yakovlev, A. L. Cavalieri, M. Uiberacker, V. Pervak, A. Apolonski, R. Kienberger, U. Kleineberg, F. Krausz, *Science* **2007**, *317*, 769.
[3] M. Kruger, M. Schenk, P. Hommelhoff, *Nature* **2011**, *475*, 78.
[4] G. Herink, D. R. Solli, M. Gulde, C. Ropers, *Nature* **2012**, *483*, 190.
[5] B. Piglosiewicz, S. Schmidt, D. J. Park, J. Vogelsang, P. Groß, C. Manzoni, P. Farinello, G. Cerullo, C. Lienau, *Nat. Photonics* **2013**, *8*, 37.
[6] F. Krausz, M. Ivanov, *Rev. Mod. Phys.* **2009**, *81*, 163.
[7] D. J. Park, B. Piglosiewicz, S. Schmidt, H. Kollmann, M. Mascheck, C. Lienau, *Phys. Rev. Lett.* **2012**, *109*, 244803.
[8] S. Kumaragurubaran, T. Takahashi, Y. Masuda, S. Furuta, T. Sumiya, M. Ono, T. Shimizu, H. Suga, M. Horikawa, Y. Naitoh, *Appl. Phys. Lett.* **2011**, *99*, 263503.
[9] W. H. Kim, C. S. Park, J. Y. Son, *Carbon* **2014**, *79*, 388.
[10] J. Yao, L. Zhong, Z. Zhang, T. He, Z. Jin, P. J. Wheeler, D. Natelson, J. M. Tour, *Small* **2009**, *5*, 2910.
[11] C. He, Z. Shi, L. Zhang, W. Yang, R. Yang, D. Shi, G. Zhang, *ACS Nano* **2012**, *6*, 4214.
[12] H. R. Park, X. S. Chen, N. C. Nguyen, J. Peraire, S. H. Oh, *ACS Photonics* **2015**, *2*, 417.
[13] L. N. Tripathi, Y. M. Bahk, G. Choi, S. Han, N. Park, D. S. Kim, *Appl. Phys. Express* **2016**, *9*, 032001.
[14] J. Keller, G. Scalari, S. Cibella, C. Maissen, F. Appugliese, E. Giovine, R. Leoni, M. Beck, J. Faist, *Nano Lett.* **2017**, *17*, 7410.
[15] M. Kim, E. Pallecchi, R. J. Ge, X. H. Wu, G. Ducournau, J. C. Lee, H. Happy, D. Akinwande, *Nat. Electron.* **2020**, *3*, 479.
[16] J. W. Han, D. I. Moon, M. Meyyappan, *Nano Lett.* **2017**, *17*, 2146.
[17] A. Javey, J. Guo, Q. Wang, M. Lundstrom, H. Dai, *Nature* **2003**, *424*, 654.
[18] X. Du, I. Skachko, A. Barker, E. Y. Andrei, *Nat. Nanotechnol.* **2008**, *3*, 491.
[19] K. Boucart, A. M. Ionescu, *IEEE Trans. Electron Devices* **2007**, *54*, 1725.
[20] F. Balestra, S. Cristoloveanu, M. Benachir, J. Brini, T. Elewa, *IEEE Electron Device Lett.* **1987**, *8*, 410.
[21] S. Nirantar, T. Ahmed, G. Ren, P. Gutruf, C. Xu, M. Bhaskaran, S. Walia, S. Sriram, *Nano Lett.* **2018**, *18*, 7478.
[22] J. W. Han, D. I. Moon, J. S. Oh, Y. K. Choi, M. Meyyappan, *Appl. Phys. Lett.* **2014**, *104*, 253506.
[23] J. W. Han, M. L. Seol, D. I. Moon, G. Hunter, M. Meyyappan, *Nat. Electron.* **2019**, *2*, 405.
[24] J.-W. Han, J. Sub Oh, M. Meyyappan, *Appl. Phys. Lett.* **2012**, *100*, 213505.
[25] W. M. Jones, D. Lukin, A. Scherer, *Appl. Phys. Lett.* **2017**, *110*, 263101.
[26] L. Pescini, A. Tilke, R. H. Blick, H. Lorenz, J. P. Kotthaus, W. Eberhardt, D. Kern, *Adv. Mater.* **2001**, *13*, 1780.

[27] J. P. Sun, G. I. Haddad, P. Mazumder, J. N. Schulman, *Proc. IEEE* **1998**, *86*, 641.
[28] M. Feiginov, C. Sydlo, O. Cojocari, P. Meissner, *Appl. Phys. Lett.* **2011**, *99*, 233506.
[29] K. J. Gan, C. S. Tsai, Y. W. Chen, W. K. Yeh, *Solid-State Electron.* **2010**, *54*, 1637.
[30] N. Jin, S. Y. Chung, R. M. Heyns, P. R. Berger, R. H. Yu, P. E. Thompson, S. L. Rommel, *IEEE Electron Device Lett.* **2004**, *25*, 646.
[31] Y. Koyama, R. Sekiguchi, T. Ouchi, *Appl. Phys. Express* **2013**, *6*, 064102.
[32] T. Maekawa, H. Kanaya, S. Suzuki, M. Asada, *Electron. Lett.* **2014**, *50*, 1214.
[33] L. Esaki, *Phys. Rev.* **1958**, *109*, 603.
[34] L. Esaki, R. Tsu, *IBM J. Res. Dev.* **1970**, *14*, 61.
[35] Z. Shi, C. B. Simmons, J. R. Prance, J. K. Gamble, T. S. Koh, Y. P. Shim, X. Hu, D. E. Savage, M. G. Lagally, M. A. Eriksson, M. Friesen, S. N. Coppersmith, *Phys. Rev. Lett.* **2012**, *108*, 140503.
[36] K. Y. Tan, K. W. Chan, M. Mottonen, A. Morello, C. Yang, J. van Donkelaar, A. Alves, J. M. Pirkkalainen, D. N. Jamieson, R. G. Clark, A. S. Dzurak, *Nano Lett.* **2010**, *10*, 11.
[37] J. Verduijn, G. C. Tettamanzi, S. Rogge, *Nano Lett.* **2013**, *13*, 1476.
[38] D. Culcer, A. L. Saraiva, B. Koiller, X. Hu, S. D. Sarma, *Phys. Rev. Lett.* **2012**, *108*, 126804.
[39] M. Amman, R. Wilkins, E. Ben-Jacob, P. D. Maker, R. C. Jaklevic, *Phys. Rev. B: Condens. Matter* **1991**, *43*, 1146.
[40] A. E. Hanna, M. Tinkham, *Phys. Rev. B: Condens. Matter* **1991**, *44*, 5919.
[41] M. Parzefall, P. Bharadwaj, A. Jain, T. Taniguchi, K. Watanabe, L. Novotny, *Nat. Nanotechnol.* **2015**, *10*, 1058.
[42] H. L. Qian, S. W. Hsu, K. Gurunatha, C. T. Riley, J. Zhao, D. Lu, A. R. Tao, Z. W. Liu, *Nat. Photonics* **2018**, *12*, 485.
[43] J. Kern, R. Kullock, J. Prangsma, M. Emmerling, M. Kamp, B. Hecht, *Nat. Photonics* **2015**, *9*, 582.
[44] W. Du, T. Wang, H.-S. Chu, C. A. Nijhuis, *Nat. Photonics* **2017**, *11*, 623.
[45] P. Wang, A. V. Krasavin, M. E. Nasir, W. Dickson, A. V. Zayats, *Nat. Nanotechnol.* **2018**, *13*, 159.
[46] H. Chalabi, D. Schoen, M. L. Brongersma, *Nano Lett.* **2014**, *14*, 1374.
[47] J. A. Misewich, R. Martel, P. Avouris, J. C. Tsang, S. Heinze, J. Tersoff, *Science* **2003**, *300*, 783.
[48] P. Rai, N. Hartmann, J. Berthelot, J. Arocas, G. Colas des Francs, A. Hartschuh, A. Bouhelier, *Phys. Rev. Lett.* **2013**, *111*, 026804.
[49] S. Namgung, D. A. Mohr, D. Yoo, P. Bharadwaj, S. J. Koester, S. H. Oh, *ACS Nano* **2018**, *12*, 2780.
[50] M. Parzefall, A. Szabo, T. Taniguchi, K. Watanabe, M. Luisier, L. Novotny, *Nat. Commun.* **2019**, *10*, 292.
[51] R. Berndt, J. K. Gimzewski, P. Johansson, *Phys. Rev. Lett.* **1991**, *67*, 3796.
[52] N. J. Halas, S. Lal, W. S. Chang, S. Link, P. Nordlander, *Chem. Rev.* **2011**, *111*, 3913.
[53] C. Ciraci, R. T. Hill, J. J. Mock, Y. Urzhumov, A. I. Fernandez-Dominguez, S. A. Maier, J. B. Pendry, A. Chilkoti, D. R. Smith, *Science* **2012**, *337*, 1072.
[54] Z. J. Li, B. Bai, C. Li, Q. Dai, *Carbon* **2016**, *96*, 641.
[55] C. Li, Z. Li, C. Ke, B. Bing, D. Qing, *Appl. Phys. Lett.* **2017**, *110*, 093105.
[56] M. Vahdani Moghaddam, P. Yaghoobi, G. A. Sawatzky, A. Nojeh, *ACS Nano* **2015**, *9*, 4064.
[57] L. Seiffert, T. Paschen, P. Hommelhoff, T. Fennel, *J. Phys. B: At., Mol. Opt. Phys.* **2018**, *51*, 134001.
[58] P. Hommelhoff, C. Kealhofer, M. A. Kasevich, *Phys. Rev. Lett.* **2006**, *97*, 247402.
[59] L. V. Keldysh, *Soviet Physics Jetp-Ussr* **1965**, *20*, 1307.
[60] P. Musumeci, L. Cultrera, M. Ferrario, D. Filippetto, G. Gatti, M. S. Gutierrez, J. T. Moody, N. Moore, J. B. Rosenzweig, C. M. Scoby, G. Travish, C. Vicario, *Phys. Rev. Lett.* **2010**, *104*, 084801.
[61] M. F. Ciappina, J. A. Perez-Hernandez, A. S. Landsman, W. A. Okell, S. Zherebtsov, B. Forg, J. Schotz, L. Seiffert, T. Fennel, T. Shaaran, T. Zimmermann, A. Chacon, R. Guichard, A. Zair, J. W. Tisch, J. P. Marangos, T. Witting, A. Braun, S. A. Maier, L. Roso, M. Kruger, P. Hommelhoff, M. F. Kling, F. Krausz, M. Lewenstein, *Rep. Prog. Phys.* **2017**, *80*, 054401.
[62] P. Dombi, Z. Pápa, J. Vogelsang, S. V. Yalunin, M. Sivis, G. Herink, S. Schäfer, P. Groß, C. Ropers, C. Lienau, *Rev. Mod. Phys.* **2020**, *92*, 66.
[63] Y. C. Chen, S. Z. Deng, N. S. Xu, J. Chen, *Appl. Phys. Lett.* **2020**, *116*, 063902.
[64] V. Dubois, S. J. Bleiker, G. Stemme, F. Niklaus, *Adv. Mater.* **2018**, *30*, 1801124.
[65] K. J. Kaltenecker, E. Krauss, L. Casses, M. Geisler, B. Hecht, N. A. Mortensen, P. U. Jepsen, N. Stenger, *Nanophotonics* **2020**, *9*, 509.
[66] J. S. Huang, V. Callegari, P. Geisler, C. Bruning, J. Kern, J. C. Prangsma, X. Wu, T. Feichtner, J. Ziegler, P. Weinmann, M. Kamp, A. Forchel, P. Biagioni, U. Sennhauser, B. Hecht, *Nat. Commun.* **2010**, *1*, 150.
[67] A. V. Eletskii, *Phys.-Usp.* **2010**, *53*, 863.
[68] W. Zhu, C. Bower, O. Zhou, G. Kochanski, S. Jin, *Appl. Phys. Lett.* **1999**, *75*, 873.
[69] T. Kim, J. S. Lee, K. Li, T. J. Kang, Y. H. Kim, *Carbon* **2016**, *101*, 345.
[70] N. O. Weiss, H. Zhou, L. Liao, Y. Liu, S. Jiang, Y. Huang, X. Duan, *Adv. Mater.* **2012**, *24*, 5782.
[71] Y. C. Chen, L. W. Liu, K. S. Zheng, J. C. She, S. Z. Deng, N. S. Xu, J. Chen, *Adv. Electron. Mater.* **2019**, *5*, 1900128.
[72] C. Li, X. Zhou, F. Zhai, Z. Li, F. Yao, R. Qiao, K. Chen, M. T. Cole, D. Yu, Z. Sun, K. Liu, Q. Dai, *Adv. Mater.* **2017**, *29*, 1701580.
[73] C. Li, K. Chen, M. Guan, X. Wang, X. Zhou, F. Zhai, J. Dai, Z. Li, Z. Sun, S. Meng, K. Liu, Q. Dai, *Nat. Commun.* **2019**, *10*, 4891.
[74] S. Zhou, K. Chen, M. T. Cole, Z. Li, J. Chen, C. Li, Q. Dai, *Adv. Mater.* **2019**, *31*, 1805845.
[75] C. Li, Y. Zhang, M. Mann, P. Hiralal, H. E. Unalan, W. Lei, B. P. Wang, D. P. Chu, D. Pribat, G. A. J. Amaratunga, W. I. Milne, *Appl. Phys. Lett.* **2010**, *96*, 143114.
[76] C. Li, Y. Zhang, M. T. Cole, S. G. Shivareddy, J. S. Barnard, W. Lei, B. Wang, D. Pribat, G. A. Amaratunga, W. I. Milne, *ACS Nano* **2012**, *6*, 3236.
[77] K. Otsuka, T. Inoue, Y. Shimomura, S. Chiashi, S. Maruyama, *Nanoscale* **2016**, *8*, 16363.
[78] R. H. Fowler, L. Nordheim, *Proc. R. Soc. London, Ser. A* **1928**, *119*, 173.
[79] E. L. Murphy, R. H. Good, *Phys. Rev.* **1956**, *102*, 1464.
[80] J. Xu, Z. Gu, W. Yang, Q. Wang, X. Zhang, *Nanoscale Res. Lett.* **2018**, *13*, 311.
[81] H. M. Wang, Z. Zheng, Y. Y. Wang, J. J. Qiu, Z. B. Guo, Z. X. Shen, T. Yu, *Appl. Phys. Lett.* **2010**, *96*, 023106.
[82] S. Kumar, G. S. Duesberg, R. Pratap, S. Raghavan, *Appl. Phys. Lett.* **2014**, *105*, 103107.
[83] V. L. Katkov, V. A. Osipov, *Appl. Phys. Lett.* **2014**, *104*, 053102.
[84] X. Wang, Y. Ouyang, X. Li, H. Wang, J. Guo, H. Dai, *Phys. Rev. Lett.* **2008**, *100*, 206803.
[85] S. Srisonphan, M. Kim, H. K. Kim, *Sci. Rep.* **2014**, *4*, 3764.
[86] G. T. Wu, X. L. Wei, Z. Y. Zhang, Q. Chen, L. M. Peng, *Adv. Funct. Mater.* **2015**, *25*, 5972.
[87] C. Zeng, E. B. Song, M. Wang, S. Lee, C. M. TorresJr., J. Tang, B. H. Weiller, K. L. Wang, *Nano Lett.* **2013**, *13*, 2370.
[88] S. Vaziri, G. Lupina, C. Henkel, A. D. Smith, M. Ostling, J. Dabrowski, G. Lippert, W. Mehr, M. C. Lemme, *Nano Lett.* **2013**, *13*, 1435.

[89] W. Mehr, J. Dabrowski, J. C. Scheytt, G. Lippert, Y. H. Xie, M. C. Lemme, M. Ostling, G. Lupina, *IEEE Electron Device Lett.* **2012**, *33*, 691.
[90] T. Georgiou, R. Jalil, B. D. Belle, L. Britnell, R. V. Gorbachev, S. V. Morozov, Y. J. Kim, A. Gholinia, S. J. Haigh, O. Makarovsky, L. Eaves, L. A. Ponomarenko, A. K. Geim, K. S. Novoselov, A. Mishchenko, *Nat. Nanotechnol.* **2013**, *8*, 100.
[91] Y. Chen, Z. Li, J. Chen, *ACS Appl. Mater. Interfaces* **2020**, *12*, 57505.
[92] P. See, D. J. Paul, B. Hollander, S. Mantl, I. V. Zozoulenko, K. F. Berggren, *IEEE Electron Device Lett.* **2001**, *22*, 182.
[93] P. See, D. J. Paul, *IEEE Electron Device Lett.* **2001**, *22*, 582.
[94] Y. X. Liao, P. F. Zhang, S. Bremner, S. Shrestha, S. J. Huang, G. Conibeer, *Adv. Funct. Mater.* **2017**, *27*, 1605348.
[95] T. P. E. Broekaert, W. Lee, C. G. Fonstad, *Appl. Phys. Lett.* **1988**, *53*, 1545.
[96] L. F. Luo, R. Beresford, W. I. Wang, *Appl. Phys. Lett.* **1989**, *55*, 2023.
[97] A. Pfenning, F. Hartmann, R. Weih, M. Emmerling, L. Worschech, S. Hofling, *Adv. Opt. Mater.* **2018**, *6*, 1800972.
[98] B. Tao, C. Wan, P. Tang, J. Feng, H. Wei, X. Wang, S. Andrieu, H. Yang, M. Chshiev, X. Devaux, T. Hauet, F. Montaigne, S. Mangin, M. Hehn, D. Lacour, X. Han, Y. Lu, *Nano Lett.* **2019**, *19*, 3019.
[99] Q. Xiang, H. Sukegawa, M. Belmoubarik, M. Al-Mahdawi, T. Scheike, S. Kasai, Y. Miura, S. Mitani, *Adv. Sci. (Weinheim, Ger.)* **2019**, *6*, 1901438.
[100] S. Lee, Y. Lee, E. B. Song, T. Hiramoto, *J. Appl. Phys.* **2013**, *114*, 164513.
[101] S. Lee, Y. Lee, E. B. Song, T. Hiramoto, *Nano Lett.* **2014**, *14*, 71.
[102] G. Yang, L. Tan, Y. Yang, S. Chen, G.-Y. Liu, *Surf. Sci.* **2005**, *589*, 129.
[103] R. Negishi, T. Hasegawa, K. Terabe, M. Aono, H. Tanaka, T. Ogawa, H. Ozawa, *Appl. Phys. Lett.* **2007**, *90*, 223112.
[104] R. Hayakawa, N. Hiroshiba, T. Chikyow, Y. Wakayama, *Adv. Funct. Mater.* **2011**, *21*, 2933.
[105] Q. Schaeverbeke, R. Avriller, T. Frederiksen, F. Pistolesi, *Phys. Rev. Lett.* **2019**, *123*, 246601.
[106] Y. Jing, S. Huang, J. Wu, M. Meng, X. Li, Y. Zhou, H. Peng, H. Xu, *Adv. Mater.* **2019**, *31*, 1903686.
[107] D. L. Klein, R. Roth, A. K. L. Lim, A. P. Alivisatos, P. L. McEuen, *Nature* **1997**, *389*, 699.
[108] T. Wagner, P. Talkner, J. C. Bayer, E. P. Rugeramigabo, P. Hanggi, R. J. Haug, *Nat. Phys.* **2019**, *15*, 330.
[109] C. Gong, H. J. Zhang, W. H. Wang, L. Colombo, R. M. Wallace, K. J. Cho, *Appl. Phys. Lett.* **2013**, *103*, 053513.
[110] J. Shewchun, V. A. K. Temple, *J. Appl. Phys.* **1972**, *43*, 5051.
[111] M. Chhowalla, D. Jena, H. Zhang, *Nat. Rev. Mater.* **2016**, *1*, 16052.
[112] A. K. Geim, I. V. Grigorieva, *Nature* **2013**, *499*, 419.
[113] M. Huang, S. Li, Z. Zhang, X. Xiong, X. Li, Y. Wu, *Nat. Nanotechnol.* **2017**, *12*, 1148.
[114] X. H. Mou, L. F. Register, A. H. MacDonald, S. K. Banerjee, *IEEE Trans. Electron Devices* **2017**, *64*, 4759.
[115] R. Yan, G. Khalsa, S. Vishwanath, Y. Han, J. Wright, S. Rouvimov, D. S. Katzer, N. Nepal, B. P. Downey, D. A. Muller, H. G. Xing, D. J. Meyer, D. Jena, *Nature* **2018**, *555*, 183.
[116] K. S. Novoselov, D. Jiang, F. Schedin, T. J. Booth, V. V. Khotkevich, S. V. Morozov, A. K. Geim, *Proc. Natl. Acad. Sci. U. S. A.* **2005**, *102*, 10451.
[117] C. X. Zhang, C. Gong, Y. F. Nie, K. A. Min, C. P. Liang, Y. J. Oh, H. J. Zhang, W. H. Wang, S. Hong, L. Colombo, R. M. Wallace, K. Cho, *2D Mater.* **2017**, *4*, 015026.
[118] Y. C. Lin, R. K. Ghosh, R. Addou, N. Lu, S. M. Eichfeld, H. Zhu, M. Y. Li, X. Peng, M. J. Kim, L. J. Li, R. M. Wallace, S. Datta, J. A. Robinson, *Nat. Commun.* **2015**, *6*, 7311.
[119] L. Britnell, R. V. Gorbachev, R. Jalil, B. D. Belle, F. Schedin, M. I. Katsnelson, L. Eaves, S. V. Morozov, A. S. Mayorov, N. M. Peres, A. H. Neto, J. Leist, A. K. Geim, L. A. Ponomarenko, K. S. Novoselov, *Nano Lett.* **2012**, *12*, 1707.
[120] G. H. Lee, Y. J. Yu, C. Lee, C. Dean, K. L. Shepard, P. Kim, J. Hone, *Appl. Phys. Lett.* **2011**, *99*, 243114.
[121] L. Britnell, R. V. Gorbachev, A. K. Geim, L. A. Ponomarenko, A. Mishchenko, M. T. Greenaway, T. M. Fromhold, K. S. Novoselov, L. Eaves, *Nat. Commun.* **2013**, *4*, 1794.
[122] A. Mishchenko, J. S. Tu, Y. Cao, R. V. Gorbachev, J. R. Wallbank, M. T. Greenaway, V. E. Morozov, S. V. Morozov, M. J. Zhu, S. L. Wong, F. Withers, C. R. Woods, Y. J. Kim, K. Watanabe, T. Taniguchi, E. E. Vdovin, O. Makarovsky, T. M. Fromhold, V. I. Fal'ko, A. K. Geim, L. Eaves, K. S. Novoselov, *Nat. Nanotechnol.* **2014**, *9*, 808.
[123] C. R. Dean, A. F. Young, I. Meric, C. Lee, L. Wang, S. Sorgenfrei, K. Watanabe, T. Taniguchi, P. Kim, K. L. Shepard, J. Hone, *Nat. Nanotechnol.* **2010**, *5*, 722.
[124] C. R. Woods, L. Britnell, A. Eckmann, R. S. Ma, J. C. Lu, H. M. Guo, X. Lin, G. L. Yu, Y. Cao, R. V. Gorbachev, A. V. Kretinin, J. Park, L. A. Ponomarenko, M. I. Katsnelson, Y. N. Gornostyrev, K. Watanabe, T. Taniguchi, C. Casiraghi, H. J. Gao, A. K. Geim, K. S. Novoselov, *Nat. Phys.* **2014**, *10*, 451.
[125] J. Xue, J. Sanchez-Yamagishi, D. Bulmash, P. Jacquod, A. Deshpande, K. Watanabe, T. Taniguchi, P. Jarillo-Herrero, B. J. LeRoy, *Nat. Mater.* **2011**, *10*, 282.
[126] M. Yankowitz, J. Xue, D. Cormode, J. D. Sanchez-Yamagishi, K. Watanabe, T. Taniguchi, P. Jarillo-Herrero, P. Jacquod, B. J. LeRoy, *Nat. Phys.* **2012**, *8*, 382.
[127] C. R. Dean, L. Wang, P. Maher, C. Forsythe, F. Ghahari, Y. Gao, J. Katoch, M. Ishigami, P. Moon, M. Koshino, T. Taniguchi, K. Watanabe, K. L. Shepard, J. Hone, P. Kim, *Nature* **2013**, *497*, 598.
[128] B. Hunt, J. D. Sanchez-Yamagishi, A. F. Young, M. Yankowitz, B. J. LeRoy, K. Watanabe, T. Taniguchi, P. Moon, M. Koshino, P. Jarillo-Herrero, R. C. Ashoori, *Science* **2013**, *340*, 1427.
[129] L. A. Ponomarenko, R. V. Gorbachev, G. L. Yu, D. C. Elias, R. Jalil, A. A. Patel, A. Mishchenko, A. S. Mayorov, C. R. Woods, J. R. Wallbank, M. Mucha-Kruczynski, B. A. Piot, M. Potemski, I. V. Grigorieva, K. S. Novoselov, F. Guinea, V. I. Fal'ko, A. K. Geim, *Nature* **2013**, *497*, 594.
[130] G. Kim, S. S. Kim, J. Jeon, S. I. Yoon, S. Hong, Y. J. Cho, A. Misra, S. Ozdemir, J. Yin, D. Ghazaryan, M. Holwill, A. Mishchenko, D. V. Andreeva, Y. J. Kim, H. Y. Jeong, A. R. Jang, H. J. Chung, A. K. Geim, K. S. Novoselov, B. H. Sohn, H. S. Shin, *Nat. Commun.* **2019**, *10*, 230.
[131] X. Xiong, M. Q. Huang, B. Hu, X. F. Li, F. Liu, S. C. Li, M. C. Tian, T. Y. Li, J. Song, Y. Q. Wu, *Nat. Electron.* **2020**, *3*, 106.
[132] A. Yangui, M. Bescond, T. Yan, N. Nagai, K. Hirakawa, *Nat. Commun.* **2019**, *10*, 4504.
[133] S. Zheng, S. Jo, K. Kang, L. Sun, M. Zhao, K. Watanabe, T. Taniguchi, P. Moon, N. Myoung, H. Yang, *Adv. Mater.* **2020**, *32*, 1906942.
[134] J. Lambe, S. L. Mccarthy, *Phys. Rev. Lett.* **1976**, *37*, 923.
[135] P. Johansson, R. Monreal, P. Apell, *Phys. Rev. B: Condens. Matter* **1990**, *42*, 9210.
[136] P. Bharadwaj, A. Bouhelier, L. Novotny, *Phys. Rev. Lett.* **2011**, *106*, 226802.
[137] A. Nevet, N. Berkovitch, A. Hayat, P. Ginzburg, S. Ginzach, O. Sorias, M. Orenstein, *Nano Lett.* **2010**, *10*, 1848.
[138] A. G. Curto, T. H. Taminiau, G. Volpe, M. P. Kreuzer, R. Quidant, N. F. van Hulst, *Nat. Commun.* **2013**, *4*, 1750.
[139] J. C. Prangsma, J. Kern, A. G. Knapp, S. Grossmann, M. Emmerling, M. Kamp, B. Hecht, *Nano Lett.* **2012**, *12*, 3915.
[140] B. Huang, S. Gao, Y. Liu, J. Wang, Z. Liu, Y. Guo, W. Lu, *Opt. Lett.* **2019**, *44*, 2330.
[141] M. Doderer, M. Parzefall, A. Joerg, D. Chelladurai, N. Dordevic, Y. Fedoryshyn, A. Agrawal, H. J. Lezec, L. Novotny, J. Leuthold, C. Haffner, in *2019 Conf. Lasers Electro-Opt.*, IEEE, San Jose, NJ, **2019**.
[142] A. K. Geim, K. S. Novoselov, *Nat. Mater.* **2007**, *6*, 183.

[143] R. R. Nair, P. Blake, A. N. Grigorenko, K. S. Novoselov, T. J. Booth, T. Stauber, N. M. Peres, A. K. Geim, *Science* **2008**, *320*, 1308.

[144] K. F. Mak, M. Y. Sfeir, Y. Wu, C. H. Lui, J. A. Misewich, T. F. Heinz, *Phys. Rev. Lett.* **2008**, *101*, 196405.

[145] L. Wu, H. Duan, P. Bai, M. Bosman, J. K. Yang, E. Li, *ACS Nano* **2013**, *7*, 707.

[146] M. Uiberacker, T. Uphues, M. Schultze, A. J. Verhoef, V. Yakovlev, M. F. Kling, J. Rauschenberger, N. M. Kabachnik, H. Schroder, M. Lezius, K. L. Kompa, H. G. Muller, M. J. Vrakking, S. Hendel, U. Kleineberg, U. Heinzmann, M. Drescher, F. Krausz, *Nature* **2007**, *446*, 627.

[147] G. Nimtz, *Found. Phys.* **2011**, *41*, 1193.

[148] K. K. Thornber, T. C. Mcgill, C. A. Mead, *J. Appl. Phys.* **1967**, *38*, 2384.

[149] P. Fevrier, J. Gabelli, *Nat. Commun.* **2018**, *9*, 4940.

[150] D. R. Ward, F. Huser, F. Pauly, J. C. Cuevas, D. Natelson, *Nat. Nanotechnol.* **2010**, *5*, 732.

[151] S. Kim, J. Jin, Y. J. Kim, I. Y. Park, Y. Kim, S. W. Kim, *Nature* **2008**, *453*, 757.

[152] M. Sivis, M. Duwe, B. Abel, C. Ropers, *Nat. Phys.* **2013**, *9*, 304.

[153] T. Rybka, M. Ludwig, M. F. Schmalz, V. Knittel, D. Brida, A. Leitenstorfer, *Nat. Photonics* **2016**, *10*, 667.

[154] M. Ludwig, G. Aguirregabiria, F. Ritzkowsky, T. Rybka, D. C. Marinica, J. Aizpurua, A. G. Borisov, A. Leitenstorfer, D. Brida, *Nat. Phys.* **2019**, *16*, 341.

[155] P. Lang, B. Ji, X. Song, Y. Dou, H. Tao, X. Gao, Z. Hao, J. Lin, *Opt. Lett.* **2018**, *43*, 5721.

[156] M. Samizadeh Nikoo, A. Jafari, N. Perera, M. Zhu, G. Santoruvo, E. Matioli, *Nature* **2020**, *579*, 534.

[157] C. Karnetzky, P. Zimmermann, C. Trummer, C. Duque Sierra, M. Worle, R. Kienberger, A. Holleitner, *Nat. Commun.* **2018**, *9*, 2471.

[158] P. Zimmermann, A. Hotger, N. Fernandez, A. Nolinder, K. Muller, J. J. Finley, A. W. Holleitner, *Nano Lett.* **2019**, *19*, 1172.

[159] R. L. Bailey, *J. Eng. Power* **1972**, *94*, 73.

[160] A. Sanchez, C. F. Davis, K. C. Liu, A. Javan, *J. Appl. Phys.* **1978**, *49*, 5270.

[161] G. Moddel, S. Grover, *Rectenna Solar Cells*, Springer, New York **2013**.

[162] A. Sharma, V. Singh, T. L. Bougher, B. A. Cola, *Nat. Nanotechnol.* **2015**, *10*, 1027.

[163] Y. Wang, K. Kempa, B. Kimball, J. B. Carlson, G. Benham, W. Z. Li, T. Kempa, J. Rybczynski, A. Herczynski, Z. F. Ren, *Appl. Phys. Lett.* **2004**, *85*, 2607.

[164] K. Kempa, J. Rybczynski, Z. P. Huang, K. Gregorczyk, A. Vidan, B. Kimball, J. Carlson, G. Benham, Y. Wang, A. Herczynski, Z. F. Ren, *Adv. Mater.* **2007**, *19*, 421.

[165] B. H. Son, D. J. Park, Y. H. Ahn, *Appl. Phys. Lett.* **2019**, *115*, 163102.

[166] B. H. Son, H. S. Kim, J. Y. Park, S. Lee, D. J. Park, Y. H. Ahn, *ACS Photonics* **2018**, *5*, 3943.

[167] Q. Ma, T. I. Andersen, N. L. Nair, N. M. Gabor, M. Massicotte, C. H. Lui, A. F. Young, W. J. Fang, K. Watanabe, T. Taniguchi, J. Kong, N. Gedik, F. H. L. Koppens, P. Jarillo-Herrero, *Nat. Phys.* **2016**, *12*, 455.

[168] K. F. Mak, J. Shan, *Nat. Photonics* **2016**, *10*, 216.

[169] A. Sushko, K. De Greve, M. Phillips, B. Urbaszek, A. Y. Joe, K. Watanabe, T. Taniguchi, A. L. Efros, C. S. Hellberg, H. Park, P. Kim, M. D. Lukin, *Nanophotonics* **2020**, *10*, 105.

[170] C. Li, X. Zhou, F. Zhai, Z. J. Li, F. R. Yao, R. X. Qiao, K. Chen, D. P. Yu, Z. P. Sun, K. H. Liu, Q. Dai, *Appl. Phys. Lett.* **2017**, *111*, 133101.

[171] M. V. Davidovich, *JETP Lett.* **2019**, *110*, 472.

[172] E. Rakhmatov, A. Alizadehkhaledi, G. Hajisalem, R. Gordon, *Opt. Express* **2020**, *28*, 16497.

[173] A. B. Shvartsburg, *Phys.-Usp.* **2007**, *50*, 37.

Chi Li is a professor in the National Center of Nanoscience and Technology, China. He received his Ph.D. in physics electronics from the School of Electronic Science and Engineering, Southeast University in 2011. His main research interests are low-dimensional materials, optoelectronics, and nanophotonics.

Qing Dai is a professor in the National Center of Nanoscience and Technology, China. He received his M.Eng. in electronic and electrical engineering from Imperial College, London, in 2007 and his Ph.D. in nanophotonics from the Department of Engineering, University of Cambridge in 2011. His main research interests are low-dimensional materials, optoelectronics, and nanophotonics.